Electrical post-fabrication tuning of aluminum Josephson junctions at room temperature

Materials for Quantum Technology

PAPER • **OPEN ACCESS**

Electrical post-fabrication tuning of aluminum Josephson junctions at room temperature

To cite this article: Christian Križan *et al* 2026 *Mater. Quantum. Technol.* **6** 036001

Materials for Quantum Technology

PAPER

OPEN ACCESS

RECEIVED
24 February 2026

REVISED
15 May 2026

ACCEPTED FOR PUBLICATION
19 June 2026

PUBLISHED
27 July 2026

Electrical post-fabrication tuning of aluminum Josephson junctions at room temperature

Christian Križan[1,*], Maurizio Toselli[1,2], Irshad Ahmad, Hadi Khaksaran, Marcus Rommel, Nermin Trnjanin, Janka Biznárová, Mamta Dahiya, Emil Hogedal, Halldór Jakobsson, Andreas Nylander, Jonas Bylander, Per Delsing and Giovanna Tancredi

Department of Microtechnology and Nanoscience, Chalmers University of Technology, SE-412 96 Gothenburg, Sweden
[1] These authors contributed equally to this work.
[2] Present address: Silicon Quantum Computing Pty Ltd UNSW Sydney, New South Wales, Australia.
[*] Author to whom any correspondence should be addressed.

E-mail: krizan@chalmers.se and christian.krizan@gmail.com

Keywords: amorphous materials, electrical tuning, frequency crowding, Josephson junctions, superconducting circuits, qubit

Abstract

Josephson junctions are key elements of superconducting quantum technology, serving as the core building blocks of superconducting qubits. We present an experimental study on room-temperature electrical tuning of aluminum junctions, showing that voltage pulses can controllably increase their resistance and adjust the Josephson energy while maintaining qubit quality factors above 1 million. We find that the rate of resistance increase scales exponentially with pulse amplitude during manipulation. Following the manipulation, the resistance increases spontaneously through contributions proportional to both the initial resistance and the preceding manipulation. We show that this spontaneous increase halts at cryogenic temperatures, and resumes again at room temperature. Using our stepwise protocol, we achieve up to a 270% increase in junction resistance, corresponding to a reduction of nearly 2 GHz of the qubit transition frequency. These results establish the achievable range, relaxation behavior, and practical limits of electrical tuning, enabling post-fabrication mitigation of frequency crowding in quantum processors.

1. Introduction

Quantum processors promise to tackle computational tasks far beyond those of classical computers, with superconducting architectures [1] leading the way. Yet, their practical realization remains constrained by persistent fabrication challenges in the nanoscopic precision required to produce reliable qubits. The key element of any superconducting qubit is the Josephson junction [2, 3], most commonly fabricated by connecting two superconducting leads by a thin dielectric oxide. The qubit transition frequencies are determined by junction properties such as its normal state resistance and its reactive environment, and can thus be engineered during the design stage. Despite advancements in the fabrication of Josephson junctions in terms of improvements in lithography, junction deposition, oxidation, evaporation, and angular deposition techniques [4–8], the state-of-the-art junction resistance spread is on the order of 2% [9] across a 50 mm wafer, corresponding to a frequency spread of about ± 50 MHz for transmon qubits. Frequency imprecision translates into spectral collisions between quantum operations [10], that is, frequency crowding. For processors with as few as $\sim$30 qubits, frequency crowding can reduce the probability of collision-free operations to below single-digit percentages [6, 11]. Scaling further to 1000 qubits is projected to demand frequency placement with only a few MHz of tolerance [11]. These fabrication constraints motivated the development of post-fabrication tuning techniques for Josephson junctions, where junction properties are modified to reach the desired qubit frequencies.

Post-fabrication tuning of qubit frequencies can be achieved by modifying the reactive environment of the junction, for example, through the modification of nearby capacitive elements [12]. An alternative approach, which is less dependent on engineering the surrounding electromagnetic reactance, is to directly tune the junction resistance. Almost universally, methods for modifying its resistance rely

on heating [13, 14]. Thermal annealing below 250 °C is generally believed to increase the resistance by growing the oxide layer using already-present chemisorbed oxygen [13, 14] or hydroxyl groups [13], with the contribution from hydroxyl groups likely to be smaller [14]. At higher annealing temperatures, the barrier growth is primarily driven by oxygen diffusion [13]. Through thermal annealing, resistance increases up to 400% and 290% have been reported for 4 μm^2 Nb-AlO_x-Nb junctions [14] and Al-AlO_x-Al junctions [15], respectively. However, thermally annealing a whole quantum processor does not allow for selectively tuning the resistance of individual junctions. This limitation pushed development towards laser annealing [10, 16, 17], which can achieve a tuning range of 15% [11, 18] within tens of seconds [11] at a success rate of about 90% [18] with a 0.3% resistance spread. Lately, electron beam heating [19] has been used to anneal junctions, demonstrating lower tuning ranges of 3% with approximately 1.5% resistance spread [20].

A rapidly growing interest is now directed towards electrical tuning, where the resistance of an individual Josephson junction is modified by applying electrical pulses to its electrodes [21–23]. Applying pulses that alternate in polarity significantly enhances the resistance increase [23], with demonstrated changes exceeding 130% [24]. These recent demonstrations underscore electrical tuning as a promising candidate for precise and selective post-fabrication tuning of superconducting qubits, motivating an investigation into its mechanisms, limits, and feasibility for fine-tuning quantum processors.

A practical complication of electrical tuning is the junction's relaxation effect. At room temperature, once the tuning process is stopped, the junction resistance does not remain at its tuned value. Instead, it increases rapidly and continues to drift with a slow decay lasting several hours. For frequency targeting in real quantum processors, this effect implies that the tuning process cannot simply be stopped when the desired resistance is reached. Therefore, reliable tuning requires a quantitative understanding of this relaxation effect.

In this work, we investigate the performance and limitations of electrical tuning on Al-AlO_x-Al Josephson junctions. We first characterize the natural aging of Josephson junctions, observing a gradual increase in junction resistances over time, and show that routine resistance measurements do not affect aging. We find that the rate of resistance change scales exponentially with the applied tuning voltage. We demonstrate that with our tuning procedure, performed entirely at room temperature, we achieve almost 100% resistance increase in 5 min. We investigate the effects of repeated tuning cycles and demonstrate cumulative resistance increases of up to 270%. We characterize the spontaneous post-manipulation resistance increase that follows the electrical tuning, and show that it scales linearly with the intentionally induced resistance change. Finally, we assess the impact of the manipulation process on transmon qubits [25] subjected to frequency tuning, and find qubit quality factors preserved above one million.

2. Samples and experimental procedures

We investigate electrical tuning in Al-AlO_x-Al Josephson junctions fabricated on intrinsic Si substrates. After chemical cleaning, an Al layer is deposited and acts as the wiring layer that is defined via optical lithography and etching. The Josephson junctions are patterned via e-beam lithography and formed with double-angle Al evaporation and in-situ oxidation. We fabricated three wafers with different oxidation doses, referred to hereafter as *low-dose*, *medium-dose*, and *high-dose*. Each wafer contains hundreds of square junctions, with electrode widths from 150 nm to 600 nm. The *low-dose* wafer was fabricated using the PICT process [26]. For completeness, it is worth mentioning that the metal films for the *low-dose* and *medium-dose* junctions were deposited using a Plassys MEB550S evaporator, and the metal films for the *high-dose* junctions were deposited in a Plassys MEB550SL3-UHV. The detailed fabrication processes can be found in [9].

It is important to note that our fabrication processes include multiple baking steps after Josephson junction deposition, shown in table C1. Previous work [23] has shown that heating modifies the resistance tunability of Josephson junctions. Thermal annealing of Nb-AlO_x-Nb junctions has been reported for temperatures and durations comparable to those experienced by our samples [14]. We therefore expect post-deposition heating to influence the tuning behavior observed here, although its quantitative impact is not addressed in this work.

2.1. Active resistance manipulation

While junctions naturally age through a passive process in which the resistance increases spontaneously over time, the resistance can also be intentionally manipulated. We refer to this process as *active* resistance manipulation. We modify the junction resistances using a bipolar voltage pulse train comprising a positive-bias square pulse, a blanking interval, a negative-bias square pulse, and a second blanking

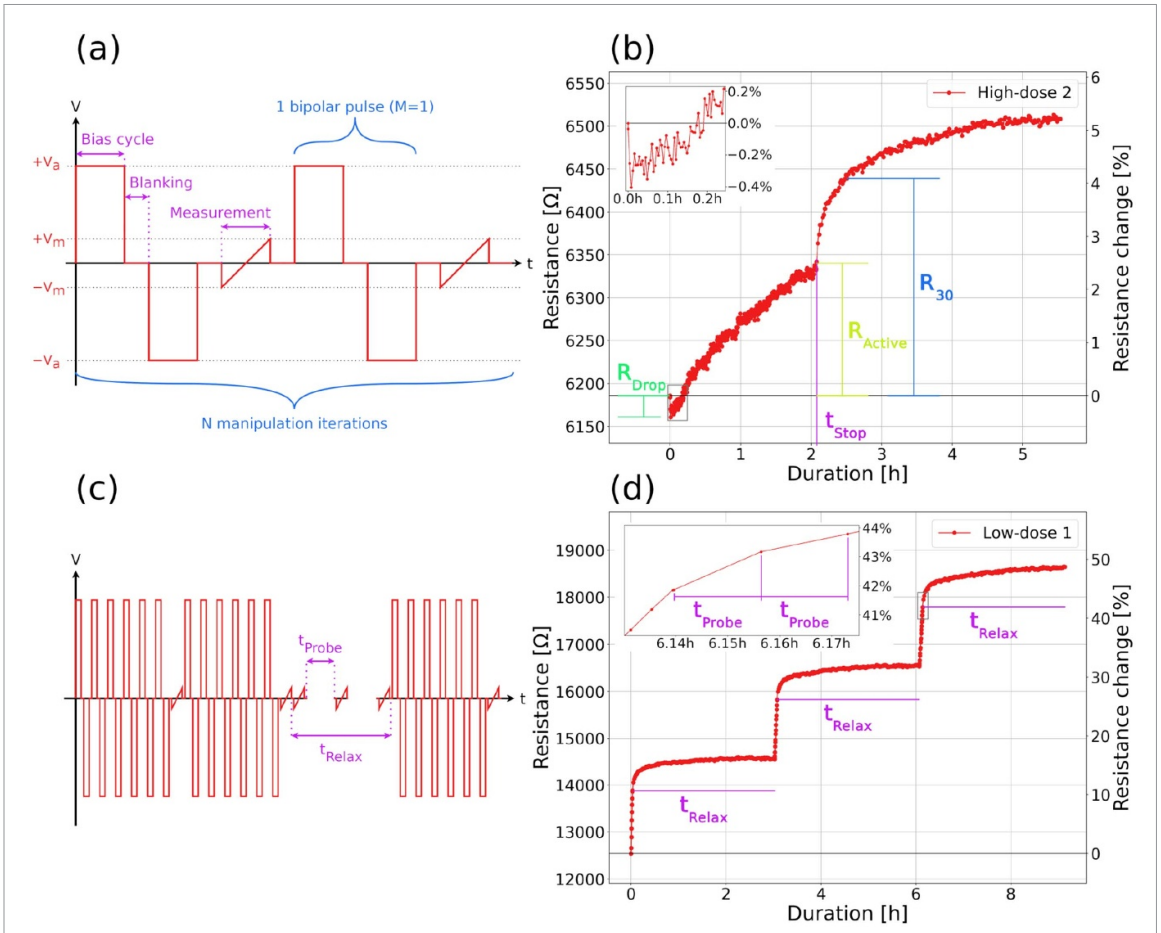

Figure 1. Active resistance manipulation of a Josephson junction using two different sequences of voltage pulses. (a) Schematic illustration of the *active* resistance manipulation protocol. (b) An example resistance trace of a junction manipulated up to the time t_{Stop} with the scheme in (a), showing the initial resistance drop, active manipulation, and subsequent relaxation. The inset shows a magnified view of the initial resistance drop. (c) Schematic illustration of the *stepped* resistance manipulation protocol in which the *active* resistance manipulation is repeated after waiting for some relaxation time t_{Relax}. During relaxation, we repeatedly measure the junction's resistance with a period of t_{Probe} between measurements. (d) Measured resistance evolution during *stepped* manipulation in (c). The insert in (d) highlights the beginning of the third relaxation event. The difference in initial resistance between (b) and (d) is explained by the difference in electrode width, despite the higher oxidation dose of the sample in (b). The electrode widths are 354 nm for (b) and 200 nm for (d). Additional sample information is provided in table 1.

interval of equal duration. We show our standard pulse sequence in figure 1(a), with figure 1(b) being an example of active resistance manipulation. No substrate heating is applied during these experiments; thermal effects are discussed separately in appendix G. The protocol closely follows the alternating-bias assisted annealing technique, with minor differences in probing and measurement [23].

As shown in figure 1(a), each manipulation experiment comprises N *iterations*, each consisting of M bipolar voltage pulses separated by a 100 ms blanking interval, followed by a resistance measurement. Unless otherwise noted, the pulse amplitude $\pm V_{\mathrm{a}}$ is set to 0.85 V, and we use $M = 6$ bipolar pulses per iteration. The duration of the square wave pulses is 200 ms, with symmetric positive and negative bias amplitudes. The resistance is extracted from an I–V measurement in which the bias voltage V_m is swept linearly from -13 mV to $+13$ mV, while monitoring the sourced current. The junction resistance is obtained from a linear fit to the I–V data. The measurement period is intentionally set to an integer multiple of $\frac{1}{50\,\mathrm{Hz}} = 20$ ms to suppress AC mains interference. Both resistance manipulation and measurement are performed using a source-measurement unit mounted to a manual probe station in a four-wire configuration, as detailed in appendix A. This setup is used for all experiments in this work, except for the aging and dielectric breakdown characterizations reported in section 3.2 and appendix H, respectively, which are instead performed using an automated probe station as described in appendix A.

Figure 1(b) shows the typical junction response during active manipulation. We observe three distinct regimes: (i) an initial decrease in resistance, denoted R_{Drop}; (ii) the active manipulation phase, during which the resistance is intentionally increased to R_{Active}; and (iii) a post-manipulation relaxation

characterized by a rapid rise followed by a long-tailed saturation after the manipulation is halted at time t_{Stop}. During this relaxation phase, the source-measurement unit remains connected to the junction to continuously monitor the resistance without applying manipulation pulses.

Active manipulation always carries the risk of breaking the junction, most commonly through the formation of a short-circuit across the junction. This breaking mechanism has been linked to the glass-like behavior in Al-AlO_x-Al Josephson junctions during annealing and relaxation [27]. This observation suggests that incorporating relaxation intervals between manipulation steps may reduce mechanical or structural strain. For this reason, we investigated *stepping* the active manipulation: we perform active resistance manipulation until a fixed increment relative to the initial resistance is reached, followed by a waiting time t_{Relax} during which the junction relaxes, after which the procedure is repeated. We refer to this protocol as *stepped* active manipulation. Figures 1(c) and (d) illustrate the waveform used for this process, and the resulting resistance changes, respectively. The results of our stepped manipulation experiments are presented in section 3.5.

2.2. Effect of resistance manipulation on qubit performance

The primary motivation of this work is to employ resistance manipulation for tuning qubit frequencies post-fabrication. We therefore investigate the impact of active manipulation on qubit decoherence and quality factor.

On the *high-dose* wafer, we fabricated two nominally identical devices, S_1 and S_2, each containing eight fixed-frequency transmon qubits $Q_1 - Q_8$. S_1 and S_2 were fabricated adjacent to one another on the wafer. We performed two cryostat cooldowns using identical device mounting positions, cabling, and instrumentation. In the first cooldown, S_1 served as a reference while S_2 underwent active resistance manipulation. Prior to the second cooldown, S_1 was manipulated, and S_2 underwent a second manipulation process. During each manipulation, the junction resistances increase, lowering the qubits' transition frequencies.

To assess qubit performance, we characterize decoherence metrics in section 3.6 by interleaving measurements of the energy relaxation time T_1, the Ramsey dephasing time T_2^*, and the Hahn-echoed dephasing time T_2^{e}. These measurements are repeated every 15 min over approximately one day per device per cooldown, with the distribution mean reported in table B2. Qubit quality factors are extracted from the measured T_1 distributions.

3. Results

We now summarize the main results of this work. We first provide an overview of the Josephson junction samples and show that the measurement process itself does not induce resistance change, while confirming that natural aging depends on junction size. We demonstrate room-temperature active resistance manipulation and model how the resistance manipulation depends on the amplitude of the tuning signal. We compare the total resistance change to the actively induced resistance change, and show that a stepped manipulation protocol extends the accessible resistance range. Finally, we assess the impact of resistance manipulation on the decoherence and quality factors of transmon qubits.

3.1. Josephson junction samples

Table 1 summarizes parameters of the Josephson junction samples studied in this work. R_W denotes the mean initial room-temperature resistances of the unmanipulated junctions. The electrode width $\sqrt{A}$ is defined assuming junctions of square cross-sections, and $R_W \cdot A$ is the corresponding resistance-area product. The oxidation parameters are the pressure p_{ox}, time t_{ox}, and dose D_{ox}, with D_{ox} being calculated using the empirical formula in [28]. *Age* specifies the time elapsed between fabrication and the first measurement, where t_0 is defined as the time of the deposition of the second junction electrode, corresponding to the junction *birth time* [27].

3.2. Aging

We characterized junction aging by monitoring the resistance spontaneously increasing under ambient laboratory conditions, with the aim of determining whether the measurement current or cadence of measurement influences aging.

Measurements were performed at room temperature using an automatic probe station, described in appendix A. The junction geometries studied here differ from those stated in table 1: the *low-dose* junctions feature electrode widths of 100 nm and 500 nm, and the *medium-dose* junctions feature widths of 200 nm and 600 nm, representing small and large devices, respectively.

Table 1. Summary of the five Josephson junction variants fabricated on three wafers of different oxidation doses, denoted as *low-dose*, *medium-dose*, and *high-dose*.

Sample	Low-dose 1	Low-dose 2	Medium-dose 1	High-dose 1	High-dose 2
R_W [Ω]	11662	5513	11057	7840	6281
$\sqrt{A}$ [nm]	200	300	350	318	354
$R_W \cdot A$ [nΩm^2]	0.47	0.50	1.35	0.79	0.79
Age [days]	>182	>359	>364	>102	>102
p_{ox} [mbar]	2	2	10	10	10
t_{ox} [min]	20	20	60	150[a]	150[a]
D_{ox} [mbar$^{0.43}$ · min$^{0.65}$]	9.4	9.4	38.5	224.0	224.0

[a] The oxidation time for the *high-dose* wafer is an estimate, due to a cleanroom power failure with no machine logs being saved for the actual time.

To characterize and quantify resistance changes we define the resistance change $\rho(t)$ as

$$\rho(t) = \frac{R(t)}{R(0)} - 1, \tag{1}$$

where $R(t)$ is the resistance measured at time t, with $R(0)$ being the initial resistance. We express $\rho(t)$ in units of % to enable comparison across junctions with different initial resistances and wafer origins. Figure 2(a) shows the natural $\rho(t)$ evolution for varying measurement currents and measurement intervals; each trace corresponds to an individual junction tracked throughout the study. Similar to earlier work [29], we observe a significant increase of $R(t)$ over a period of two weeks. We find no significant difference in aging behavior between frequently and infrequently measured samples, indicating that the resistance measurements do not measurably affect aging. Hence, we can assume that junctions can be measured safely without the junction changing its resistance beyond the extent it would have changed normally due to natural aging. While the data suggest slower aging for *medium-dose* junctions compared to *low-dose* junctions, a definitive comparison is precluded by differences in the experimental conditions. In particular, measurements of the *medium-dose* junctions began 19 days after deposition, compared to 2 days for the *low-dose* junctions, and the *medium-dose* junctions were additionally subjected to post-deposition heating, which is expected to mitigate subsequent aging.

Figure 2(b) shows $\rho(t)$ as a function of junction size. Each data point represents an average over measurements performed at bias currents of 25 nA, 50 nA, 100 nA, and 1 μA; for *low-dose* junctions, measurements at 10 μA were also included. Each data point is the average of all resistance measurements on the last day in figure 2(a), corresponding to ages of 16 (32) days for *low-dose* (*medium-dose*) junctions. Independent of oxidation dose, smaller junctions exhibit faster aging. This trend is consistent with previous reports of size-dependent resistance change in Nb-Al-AlO$_x$-Nb junctions [13], although in that case the normal-state resistance was observed to decrease over time.

Overall, our observations indicate (i) the resistance spontaneously increasing by several tens of percent over a time scale of a month, (ii) faster aging for smaller junctions, (iii) no measurable influence of the measurement currents or measurement cadence on the aging process, and (iv) no conclusive difference in aging across oxidation doses within the constraints of this study.

3.3. Active manipulation

We manipulate the junction resistance by applying a train of voltage pulses, as shown in figure 1(a). Figures 3(a)–(e) show the actively induced $\rho(t)$ as a function of time for different pulse amplitudes V_a, measured across the five Josephson junctions variants listed in table 1. Across all devices, we find that an increasing V_a yields a higher rate of resistance change over time, with a maximum increase of 96.2% achieved in 5 min.

We fit the active resistance manipulation to a second-order polynomial equation

$$\rho(t) = \alpha(V) \cdot t + \beta(V) \cdot t^2, \tag{2}$$

where $\alpha(V)$ and $\beta(V)$ quantify the linear and quadratic time dependencies, respectively. The second-order polynomial was chosen empirically based on a comparison between four different candidate models, discussed in appendix E. The fit is restricted to the active manipulation regime shown in figure 1(b); prior to fitting, we remove the initial resistance drop, as illustrated in figures 3(f) and (g) and discussed further in appendix E.1.

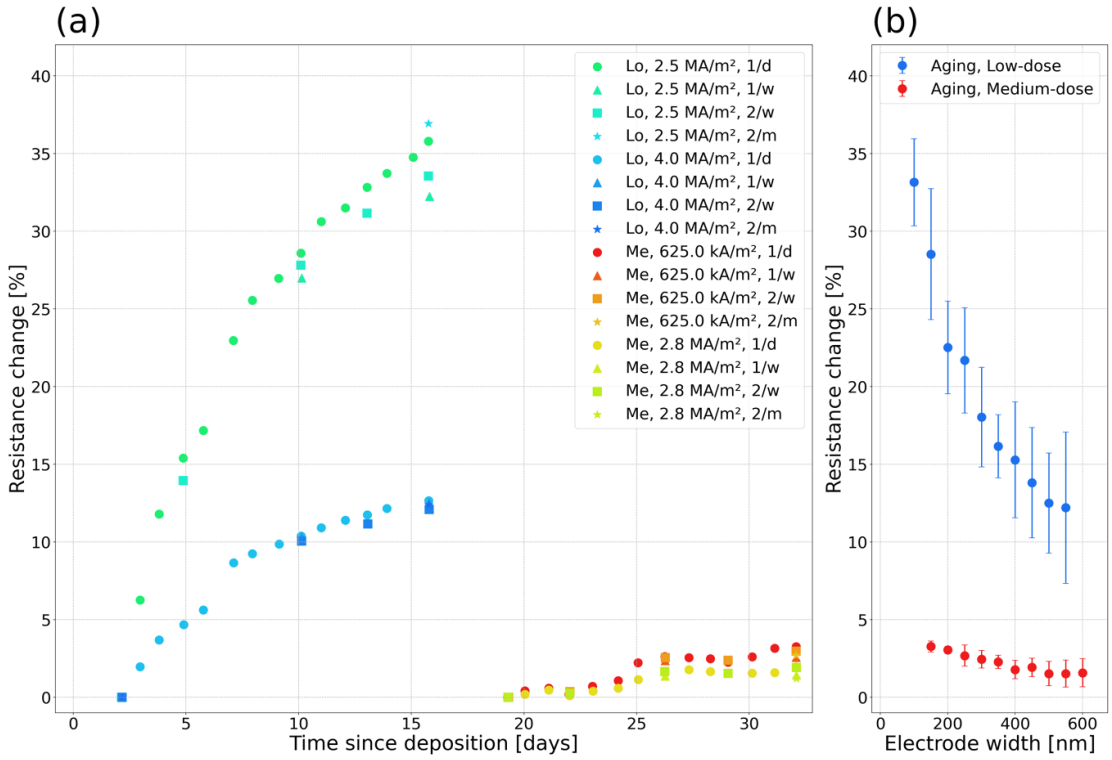

Figure 2. Natural aging of *low-dose* and *medium-dose* junctions of different sizes, denoted as *Lo* and *Me*, respectively. (a) Resistance change $\rho(t)$ as a function of time measured at different probe currents and measurement intervals; *1/d*: daily, *1/w*: weekly: *2/w*: biweekly, *2/m*: bimonthly. The legend indicates the measurement current density I/A. Adapted from [43] with permission. (b) Resistance change $\rho(t)$ of *low-dose* and *medium-dose* junctions as a function of junction electrode width. The *low-dose* data were measured 2 days after fabrication, and the *medium-dose* data after 19 days. When normalized to the earliest data point, the *medium-dose* junctions appear to age more slowly, likely reflecting them being 17 days older when measured. Adapted from [43] with permission.

Figure 4 shows the parameters obtained from fitting the data in figures 3(a)–(e) with equation (2). Figure 4(a) shows the linear coefficient $\alpha(V)$ as a function of the manipulation pulse amplitude for the different samples. We find that $\alpha(V)$ exhibits an exponential dependence on voltage, which we model as

$$\alpha(V) = \alpha_0 \cdot \mathrm{e}^{V/V_0}, \tag{3}$$

where V_0 is the characteristic voltage corresponding to an e-fold increase in $\alpha(V)$, with α_0 being a prefactor modifying the voltage sensitivity. The extracted parameters are listed in table 2; increasing the pulse amplitude by approximately 200 mV results in at least an order-of-magnitude increase in the resistance-change rate for the *low-dose* and *high-dose* junctions, whereas the *medium-dose* junctions exhibit a more modest increase of about a factor of two over the measured range. Figure 4(a) also shows that samples from the same wafer cluster according to their resistance-area product $R_W \cdot A$, rather than junction area. This observation is consistent with previous reports indicating that electrical tuning exhibits only weak dependence on junction area [23]. Furthermore, the *medium-dose* manipulation results show that $R_W \cdot A$ alone is not sufficient to predict the exponential voltage dependence. Although $\alpha(V)$ appears smaller for larger $R_W \cdot A$, the *medium-dose* sample deviates from this trend, exhibiting an intermediate $\alpha(V)$ despite its comparatively large resistance-area product. As seen in table 2, the prefactor α_0 spans over three orders of magnitude across the junctions while the extracted characteristic voltage V_0 lies in the range 55–91 mV. Interestingly, these values are higher but comparable to the thermal voltage at room temperature, $V_T \equiv k_B T/e \approx 25$ mV, consistent with slow resistance changes due to aging at room temperature. Within error bars, we also observe that V_0 remains constant between junction variants on a particular wafer, leaving α_0 to capture variations in α between samples.

Figure 4(b) shows the quadratic coefficient $\beta(V)$ extracted from equation (2). The values of $\beta(V)$ are predominantly negative, consistent with a $R(t)$ increasing slower over time; occasional positive values are close to zero and are attributed to fitting uncertainty. Since the quadratic term ultimately dominates at long times, we estimate the crossover time at which $\beta(V)\,t^2$ surpasses $\alpha(V)\,t$. Across all junctions in figure 4, this time has a median of 26 min and a mean of 50 min, meaning that $\alpha(V)$ remains the dominant source of resistance change for the timescales observed in this study. The observation also implies

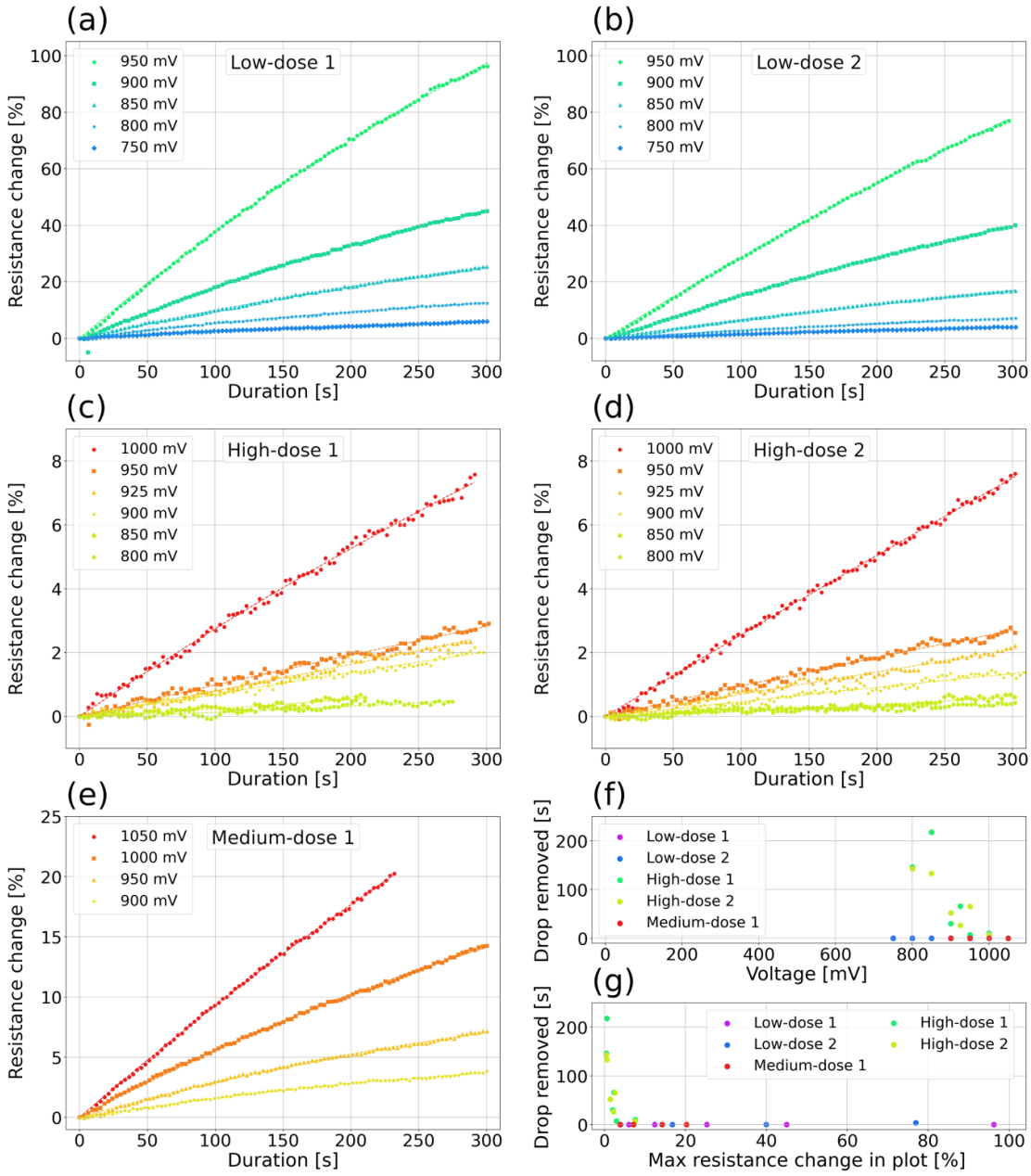

Figure 3. Resistance change during active manipulation at multiple pulse amplitudes for (a) *low-dose 1*, (b) *low-dose 2*, (c) *high-dose 1*, (d) *high-dose 2*, and (e) *medium-dose 1* junctions. Manipulation at voltages exceeding the highest value shown in each panel resulted in junction failure. The time-dependent resistance change is dominated by a linear term $\alpha(V)$ with a quadratic contribution $\beta(V)$, as defined in equation (2). (f) and (g) show the duration of the manually excluded initial resistance drop for each device set in (a)–(e), as a function of the manipulation voltage (f) and the maximum resistance change (g).

the existence of a time where the resistance stops changing, assuming a hypothetical junction that survives active resistance manipulation for dozens of minutes.

Figures 4(c)–(e) compare $\alpha(V)$ and $\beta(V)$, and weakly suggest an anticorrelation between the two parameters, with larger $\alpha(V)$ accompanied by more negative $\beta(V)$. Physically, this trend implies that faster resistance changes are associated with more rapid deceleration of the tuning process: if a junction changes its resistance faster than before, then it would stop changing its resistance sooner. However, the limited data set precludes a statistically significant quantification of this relationship.

3.3.1. The initial drop in resistance

As was shown in figure 1(b), we observe an initial decrease in resistance at the onset of active manipulation, consistent with previous reports [30]. The duration and magnitude of this drop are sample-dependent. In aged *low-dose* and *medium-dose* junctions, the effect is typically weak and limited to one or two data points, as shown in figures 3(f)–(g). In contrast, aged *high-dose* junctions exhibit a

Table 2. Parameters α_0 and V_0 as extracted by fitting the data in figure 4(a). The % denotes the relative resistance change.

	Low-dose 1	Low-dose 2	Medium-dose 1	High-dose 1	High-dose 2
α_0 [10^{-9} %/s]	824 ± 351	420 ± 271	1002 ± 531	0.79 ± 1.19	0.37 ± 0.37
V_0 [mV]	72.5 ± 2.4	70.4 ± 3.4	91.4 ± 4.3	57.5 ± 5.0	55.3 ± 3.1

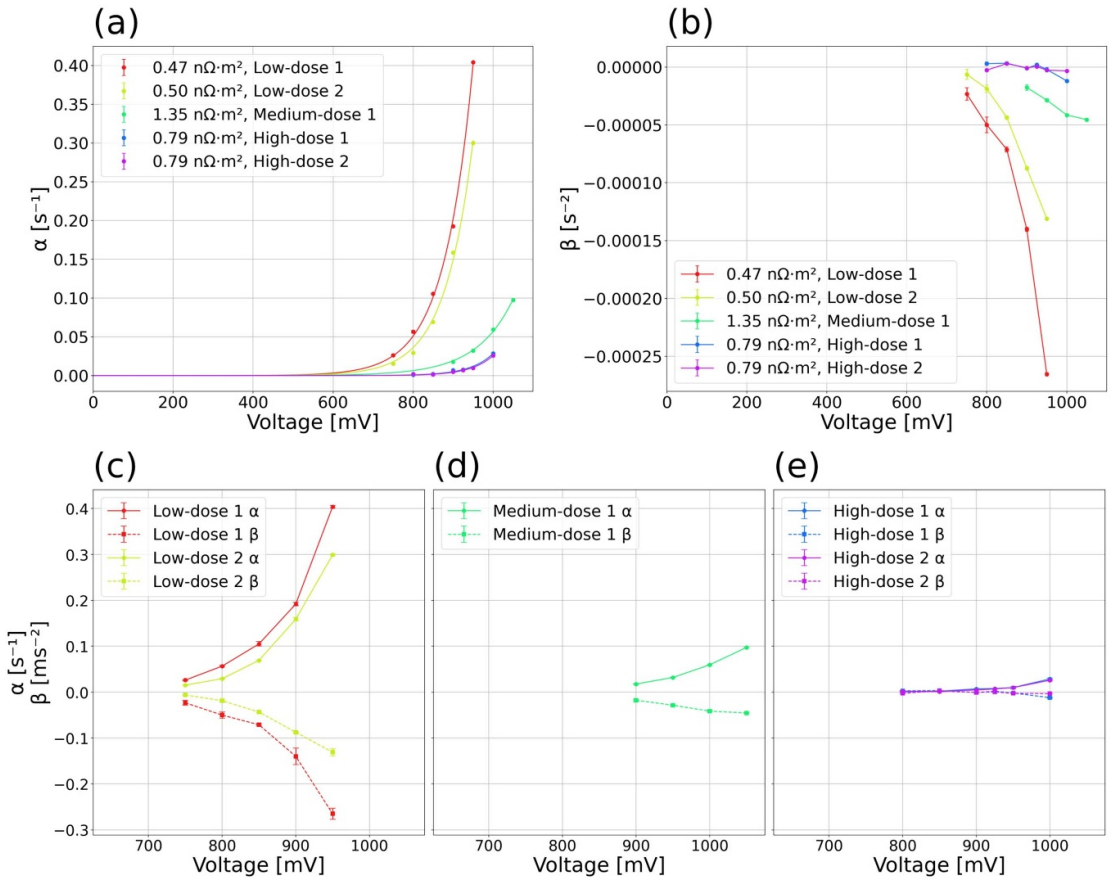

Figure 4. Extracted parameters (a) $\alpha(V)$ and (b) $\beta(V)$ obtained by fitting equation (2) to the resistance traces in figure 3. Panels (c)–(e) compare the voltage dependence of $\alpha(V)$ and $\beta(V)$. The linear coefficient $\alpha(V)$ exhibits an exponential dependence on voltage. The resistance-area product $R_N A$ [nΩm^2] for the five junction variants is indicated in the legends of (a) and (b).

pronounced and extended resistance drop under comparable manipulation conditions. Performing the stepped active manipulation experiment outlined in section 2.1 also amplifies the initial resistance drop between iterations of the experiment, shown in figure E1.

3.4. Relaxation dependence on active manipulation

Figure 1(b) shows that the junction has increased its resistance by R_{Active} when active manipulation ceases at a time t_{Stop}, corresponding to a relative change ρ_{Active}; however, the junction's resistance continues to increase due to a relaxation mechanism up to a value R_{Total}, giving a relative change ρ_{Total}. It has been reported that, when the active manipulation is stopped, the relaxation mechanism adds a fixed fraction of the initial resistance independently of how much the resistance was increased during active manipulation [30]. Under this observation, a plot of ρ_{Total} as a function of ρ_{Active} should yield a linear relation with unit slope and a finite offset. The offset quantifies the amount of resistance change after manipulation, independent of the active resistance change introduced during manipulation.

To test this behavior across different junction variants, we performed active manipulation to varying values of ρ_{Active}, measured the corresponding ρ_{Total}, and made a linear fit to the data. As the relaxation process follows a logarithmic time dependence and therefore lacks a well-defined asymptote here, we define the resistance measured 30 min after the manipulation is halted as $R_{30} = R(t_{\text{Stop}} + 30\,\text{min})$, and consider the total resistance change $\rho_{\text{Total}}(t = 30\,\text{min}) = \frac{R_{30}}{R(0)} - 1$.

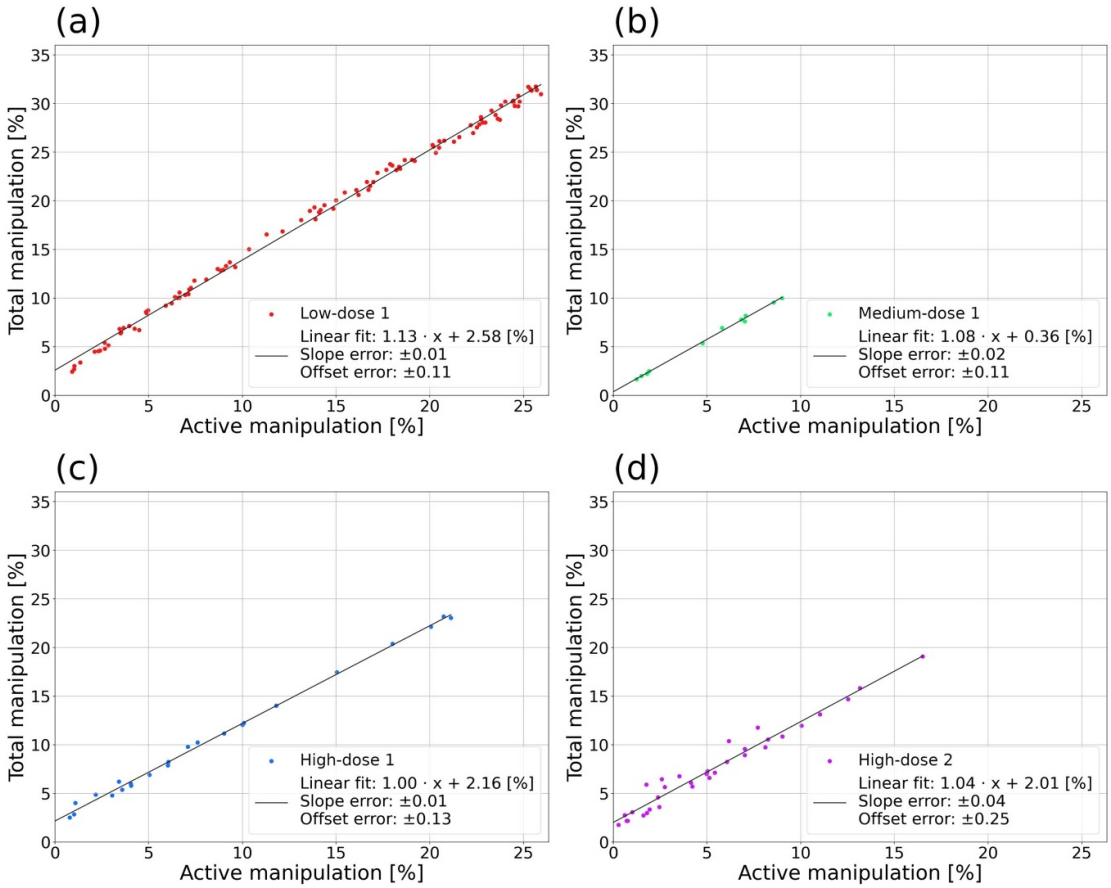

Figure 5. Linear fit of the resistance change 30 min after manipulation, as a function of the *active* resistance change for (a) *low-dose 1*, (b) *medium-dose 1*, (c) *high-dose 1*, and (d) *high-dose 2* junctions. Each datapoint corresponds to one independent manipulation and relaxation. A slope of unity indicates that the relaxation contributes a fixed resistance increase offset independent of the actively induced resistance change.

Figure 5 shows the resistance change $\rho_{\mathrm{Total}}(t)$ at $t = 30\,\mathrm{min}$ as a function of the actively induced change ρ_{Active} for the (a) *low-dose 1*, (b) *medium-dose 1*, (c) *high-dose 1* and (d) *high-dose 2* junctions. The data is fitted with $\rho_{\mathrm{Total}}(t = 30\,\mathrm{min}) = k\,\rho_{\mathrm{Active}} + m$. The *high-dose* samples reproduce the previously reported behavior, with fitted slopes k of 1.00 ± 0.01 and 1.04 ± 0.04, for *high-dose 1* and *high-dose 2*, respectively. In contrast, *low-dose 1* and *medium-dose 1* exhibit larger k of 1.13 ± 0.01 and 1.08 ± 0.02, respectively, indicating manipulation-dependent relaxation. We attribute these deviations in k to physical effects rather than systematic error, given the goodness of fit, low scatter, and the identical measurement protocol yielding unit slopes for the high-dose devices. Moreover, the fitted offsets m differ across all samples, suggesting that relaxation is governed by intrinsic material properties.

As shown in figure 1(b), the resistance change due to relaxation is not instantaneous. While figure 5 establishes a linear relationship between ρ_{Active} and $\rho_{\mathrm{Total}}(t = 30\,\mathrm{min})$, predicting the relaxation of a given junction variant requires determining whether this relationship changes over time. We therefore examined how the parameters k for the slope and m for the offset extracted from the linear fit between ρ_{Total} and ρ_{Active} evolve with the time elapsed after manipulation. We measure the resistance at different times, $R(t_{\mathrm{Stop}} + \tau)$, with τ ranging from 0 h to 24 h, and evaluate $\rho_{\mathrm{Total}}(\tau) = \frac{R(t_{\mathrm{Stop}}+\tau)}{R(0)} - 1$. At each time step, we perform a linear fit and extracted the values of the slope k and offset m as a function of τ. This analysis was performed on the *low-dose 1* junctions, for which the largest data set was available. The results are reported in figure 6 and show that neither the slope nor the offset stabilizes within 24 h. To be able to model the relaxation over time, we fit the time dependence of k and m empirically to a logarithmic growth function,

$$y(t) = a + b \cdot \ln(1 + t/\tau)\,. \tag{4}$$

The logarithmic model was selected over a power-law fit, following a comparison reported in appendix F. The extracted fit parameters are shown in the legends.

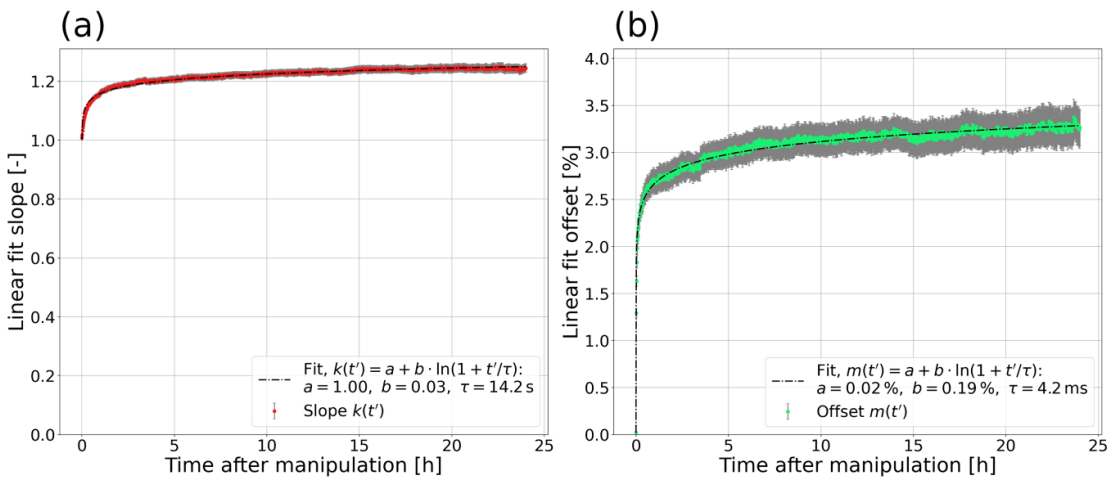

Figure 6. Time dependence of the slope k (a) and offset m (b) extracted from linear fits at different times τ after manipulation of $\rho_{\text{Total}}(\tau) = k\,\rho_{\text{Active}} + m$. An example fit where $\tau = 30$ min is shown in figure 5(a).

Figure 6(a) shows how parameter k changes as a function of the time elapsed after manipulation is halted. We find that, in addition to the fixed relaxation offset observed independently of the magnitude of active manipulation, the relaxation process contributes with approximately one quarter of ρ_{Active} to ρ_{Total}. This result demonstrates that the relaxation is not always independent of the active manipulation. The amount of $\rho(t)$ gained during relaxation, due to the amount of active resistance manipulation made, is comparable in magnitude to the frequency tolerances required for tuning quantum processors. Figure 6(b) shows that the $\rho(t)$ acquired from relaxation, regardless of the active manipulation, is $3.29 \pm 0.19\%$. The uncertainty of $\pm$ 0.19% is particularly relevant for qubit frequency targeting: as estimated in appendix D.1, this uncertainty sets a lower bound of 11.3 MHz on the achievable qubit frequency precision, about five times better than the regular fabrication precision. These results have direct practical implications for post-fabrication tuning: both k and m of the relaxation process must be characterized to achieve accurate electrical tuning, requiring multi-day monitoring of statistically significant ensembles of sacrificial junctions.

3.5. Stepped active manipulation

We now demonstrate that stepped active manipulation can increase $\rho(t)$ beyond the 96% achieved with regular active manipulation. The pulse sequence for the stepped scheme is shown in figure 1(c). Figure 7 presents the resistance evolution of a *low-dose 1* junction, aged 348 days at the time of measurement, as it is subjected to successive manipulation steps. Using this protocol, we increase the junction resistance by 269.5%, which, to our knowledge, is the largest resistance change reported for an individually targeted Josephson junction, corresponding to a transmon qubit shifting its frequency by $\Delta f = -1964$ MHz. Upon further stepping, the junction ultimately fails during the initial resistance drop of the final manipulation step. We observe that the rate of resistance change decreases with each successive step. At the same time, the magnitude of the initial resistance drop increases between steps, as shown in figure E1, to which we are unable to offer an explanation at this time.

Figure 8(a) shows the relaxation response normalized to the initial resistance at the beginning of the experiment $R(t = 0)$, where each trace corresponds to the relaxation phase of a single manipulation step in figure 7. All steps exhibit similar relaxation dynamics, following an approximately logarithmic time dependence. The main difference between steps is that the relaxation traces are progressively shifting towards higher resistance values with each successive manipulation step. Figure 8(b) shows the junction's resistance increase during each relaxation phase, measured at the 30 min and 180 min markers in figure 8(a) as a function of time since the start of the stepped manipulation. The data reveal that the speed of the resistance increase grows with successive steps, suggesting that relaxation from earlier steps persists and contributes to subsequent relaxation phases.

3.6. Decoherence and qubit quality factors

We study the effect of resistance manipulation on qubit coherence and quality factors using two devices, S_1 and S_2, each containing eight fixed-frequency transmon qubits $Q_{1..8}$. The chips were fabricated on the

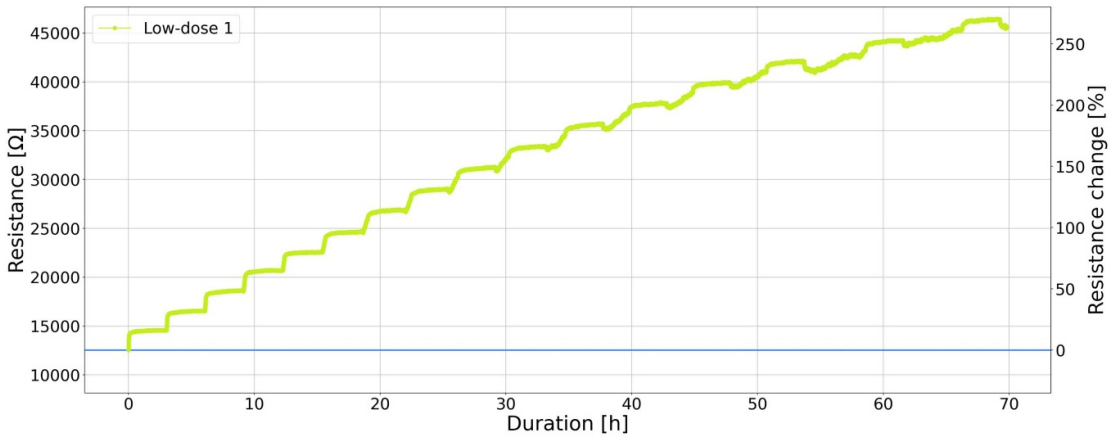

Figure 7. Stepped active manipulation of a 200 nm *low-dose* junction. Each step consists of an active resistance manipulation sequence that increases the junction resistance by $+0.10 \cdot R(0)$, followed by a 3 h relaxation period. The steps are repeated until junction failure, achieving a resistance change of $\rho = +270\%$. Using equation (D.4), this resistance change corresponds to a transmon frequency shift of $\Delta f = -1964$ MHz.

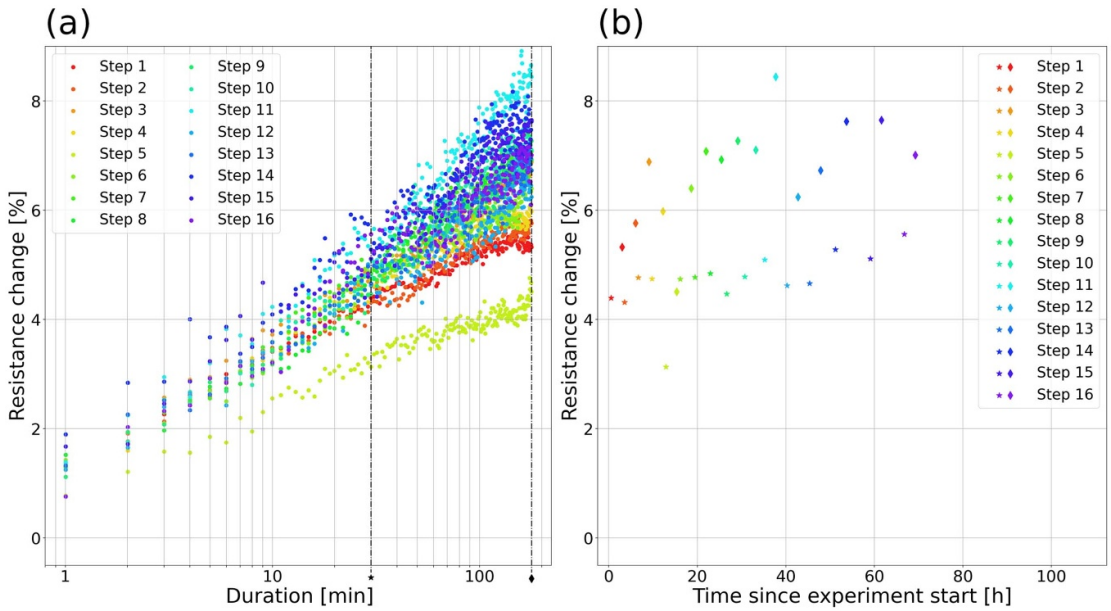

Figure 8. Analysis of relaxation during the stepped active manipulation in figure 7. (a) Lin-log$_{10}$ plot of the relative resistance change ρ during relaxation after each manipulation step in figure 7, confirming a logarithmic growth with time. Subsequent relaxation traces mainly follow the same time dependence as the first relaxation event, indicating repeated activation of the same relaxation process rather than a new one for each manipulation. (b) Relative resistance change ρ evaluated at the 30 min and 180 min markers indicated in (a) as dashed vertical lines and shown as stars and diamonds, respectively. The increasing slope across steps indicates a growing relaxation rate with successive manipulations, suggesting that ongoing relaxation from previous steps accumulates.

high-dose wafer, with qubits $Q_{1..4}$ having *high-dose 1* junctions, and qubits $Q_{5..8}$ having *high-dose 2* junctions. During the first cooldown, S_1 was measured as-fabricated, while S_2 underwent resistance manipulation. In the second cooldown, both devices were manipulated, producing a 'single-tuned' S_1 and a 'double-tuned' S_2. The qubits' junctions were manipulated using the manipulation procedure described in section 2.1.

The qubit quality factors are calculated as $Q = 2\pi f_{01} \cdot T_1$ where f_{01} is the qubit frequency, and T_1 its energy relaxation time measured during the two cooldowns. The measured f_{01}, T_1 and calculated Q values are reported in tables B1 and B2. Here, we acquire T_1, T_2^* and T_2^e using decoherence time experiments [31], performing interleaved $T_1 - T_2^* - T_2^e$ measurements and reporting the mean values together with their uncertainties. We describe our fitting procedures in [32].

Figure 9(a) shows qubit quality factors as a function of ρ_{Active} reached prior to each cooldown, denoted *C1* and *C2*, respectively. Red symbols indicate the unmanipulated reference sample S_1 while

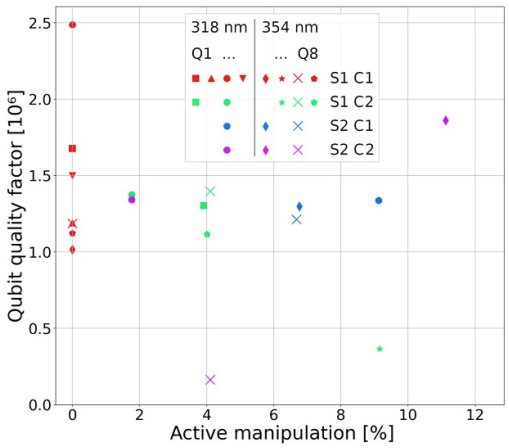

Figure 9. Qubit quality factor as a function of the active resistance manipulation. Each symbol shape denotes the same qubit across measurements. With a few exceptions, the qubit quality factors lie between $1 \cdot 10^6$ and $1.5 \cdot 10^6$ for one round of manipulation, comparable to those obtained with our standard fabrication process.

green symbols show S_1 after a single round of manipulation. Blue symbols correspond to the nominally identical sample S_2, manipulated once before *C1*, and purple symbols indicate S_2 after a second manipulation round prior to *C2*. We find that a single round of resistance manipulation preserves qubit performance, with Q values between 1 and 1.5 million, comparable to our previously reported devices [6]. Data following two manipulation rounds are inconclusive, with Q_5 increasing in quality factor after major additional tuning, and Q_7 decreasing in quality factor after minor additional tuning.

While resistance manipulation was successfully performed on most qubits, a fraction broke during the procedure. Electrostatic discharge is unlikely the cause, as manipulation was initiated and sustained on all qubits for some time. Notably, failures occurred predominantly early in the process, with approximately half of the failures occurring within the first 6 min as shown in appendix H. We attribute the elevated failure rate primarily to fabrication issues in the *high-dose* wafer. This wafer was produced using a newly commissioned evaporator for which the fabrication process had not yet been optimized; subsequent analysis revealed a less uniform deposition rate compared to other wafers studied here. Similarly, we note that $R_W \cdot A$ of the *high-dose* junctions being $0.79\,\mathrm{n\Omega m^2}$, is lower than that of the *medium-dose 1* junctions, which measured $0.87\,\mathrm{n\Omega m^2}$ 19 days after deposition. This difference can thus not be attributed to aging, and suggests that fabrication-dependent factors have contributed to either the lower $R_W \cdot A$ of the *high-dose* wafer; or, the higher $R_W \cdot A$ of the *medium-dose* wafer, for instance from its additional thermal exposure during fabrication. Additional dielectric breakdown data for junctions from this wafer are presented in appendix H. Further work is needed to distinguish whether failures stem from the manipulation protocol or wafer-specific defects.

4. Discussion and conclusion

In conclusion, we demonstrate a feasible method for manipulating the resistance of Josephson junctions. By studying multiple junction variants differing in size and oxidation dose, we confirm that natural aging is junction-size dependent, with smaller junctions aging more, and that resistance measurements performed at intervals ranging from daily to bimonthly do not measurably affect aging. We confirm earlier reports that the junction resistance can be actively increased at room temperature using electrical voltage pulses [33]. We find that the induced increase in resistance follows a second-order time dependence dominated by its linear rate by two orders of magnitude. Crucially, we find that the linear rate depends exponentially on pulse amplitude, increasing by a factor of e for every additional 55–91 mV depending on the sample. Our data show that the resistance-area product alone does not predict the voltage dependence of the rate of resistance change, with one dataset disrupting an otherwise clear negative relationship.

Contrary to previous observations [30], the resistance gained from relaxation is not always a fixed fraction of the initial junction resistance. We find that this post-relaxation resistance change can increase with the amount of active manipulation made. During relaxation, the amount of resistance change gained from active manipulation, and gained passively from the relaxation process, both scale linearly with the initial resistance, with the latter showing a partial dependence on the former. We show that

relaxation has a logarithmic time dependence regardless of the active manipulation, indicating that a manipulated sample at room-temperature requires monitoring over several hours to reliably extract relaxation parameters. The resulting uncertainty limits the achievable frequency precision of electrical tuning, which we estimate to be at least 11.3 MHz, and can possibly be reduced with greater control of the relaxation mechanism. We introduce a stepped active manipulation scheme that extends the accessible resistance range, achieving a total increase of up to 270% for an aged 12.5 kΩ junction at room temperature, the largest targeted resistance manipulation reported to date. We find that repeated steps amplify the initial resistance drop, an effect to which we currently offer no conclusive explanation. Moreover, repeated resistance manipulation steps leave cumulative effects in subsequent relaxation phases: the resistance change measured at a fixed time after each relaxation onset, shows yet a gradual increase as the stepped manipulation experiment progresses. Finally, we show that performing resistance manipulation on qubits does not degrade their performances, preserving quality factors above 1 million that are comparable to our standard fabrication outcomes. We do not observe any systematic dependence of qubit quality factors on the manipulation process.

As superconducting quantum processors continue to scale, techniques enabling rapid, selective post-fabrication correction become increasingly critical. Electrical tuning provides a promising route, and this work clarifies both its capabilities and its practical limitations.

4.1. Open questions and future experiments

Multiple open questions remain that warrant further investigation. Future work should clarify how resistance manipulation affects junction parameters most relevant for qubit frequency targeting, namely the superconducting gap $\Delta_g(T)$, the charging energy E_C, and the room-temperature to cryogenic resistance ratio R/R_N, discussed in appendix D.

While we find the rate of junction resistance increase exponentially dependent on voltage amplitude, systematic studies of other waveform parameters, such as pulse duration, asymmetry, bandwidth-induced overshoot, and shape, are warranted. Similarly, the dependence of the relaxation process on the manipulation voltage merits investigation. Complementary studies of dielectric properties before and after tuning, including breakdown voltage measurements, would provide insight into possible dielectric modifications induced by manipulation.

To assess contemporary speculations on whether the resistance manipulation is related to Cabrera–Mott oxidation, one could carefully increase the resistance until it plateaus, and subsequently apply a higher pulse amplitude to test whether resistance manipulation resumes. Theory suggests [34] that the resistance change would stagnate once an oxide film grows to a thickness where the electric field across it becomes too weak to sustain further growth; a revived resistance increase would suggest an oxide growth driven by an electric-field intensity. Similarly, the physical origin of the initial resistance drop remains unclear; the stepped active manipulation introduced here offers a promising route to isolating this effect as the drop increases with step count. Finally, extrinsic factors such as junction age and area should be disentangled by comparing relaxation slopes and offsets across same-wafer devices differing only in these parameters.

Acknowledgments

For additional insights assisting this work, we thank Daryoush Shiri for his expertise in superconductivity and Anuj Aggarwal for discussions on quantum device design. We thank William Oliver at MIT for valuable insights and discussions regarding the possible physical mechanism behind electrical tuning and its similarities to natural aging. We thank Jürgen Lisenfeld at KIT for helpful discussions on electrical tuning and for suggesting the experiment where a Josephson junction is rapidly submerged in liquid nitrogen during relaxation, which we present in the appendix.

We acknowledge financial support from the Knut and Alice Wallenberg Foundation (KAW) through the Wallenberg Center for Quantum Technology (WACQT), and in part from the EU Flagship on Quantum Technology under project HORIZON-CL4-2022-QUANTUM-01-SGA Grant 101113946 OpenSuperQPlus100. The devices were fabricated at the Myfab Chalmers Nanofabrication Laboratory.

Data availability statement

The data that support the findings of this study are openly available at the following URL/DOI: https://dx.doi.org/10.5281/zenodo.17817323 [47].

Conflict of interest

A.N. and M.R. are board members and shareholders of Arkeon Technologies AB. The other authors declare no competing interests.

Appendix A. Experimental setup

The room-temperature resistance manipulation and measurements were performed using a Keysight B2902B source-measurement unit, connected to a Keyfactor SimplePS manual probe station equipped with MPI MP40 probes and PT-W-S-2MIC tungsten needles. All measurements were conducted in an electrostatic discharge-protected area, with an Ion Systems 6430 ionizer fan continuously directed at the sample being manipulated. Aging and dielectric breakdown measurements were carried out in an MPI TS2000-D automated probe station, using a Keithley 2612B System SourceMeter and a Keithley 3706A-S System Switch for sample multiplexing.

The microwave setup used for qubit characterization is illustrated in figure A1. The samples were thermalized at the 10 mK stage of a Bluefors LD250 dilution refrigerator with highly-attenuated RF lines. Samples S_1 and S_2 share the same input/output readout line for all experiments, using coaxial microwave switches. Waveform generation and readout are handled using an IMP Presto-16-QC-DC AWG lock-in amplifier [35, 36]. The samples, illustrated in figure A2, consist of 8 fixed-frequency transmon qubits whose readout resonators share a common feedline. The device parameters are given in table B1.

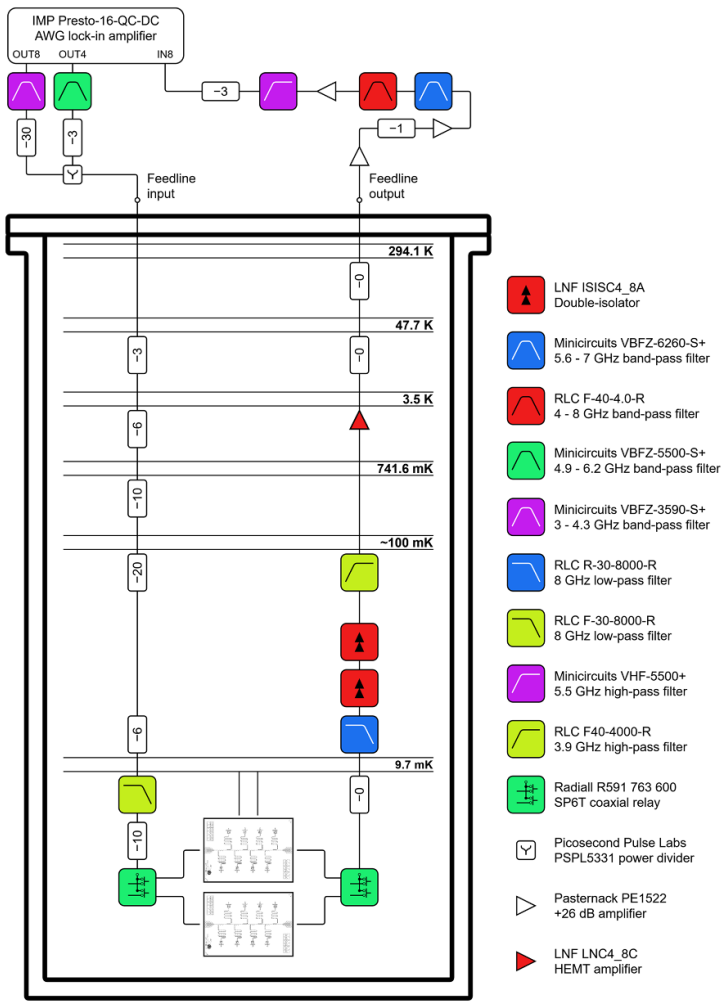

Figure A1. Full wiring diagram for the experimental setup. The numbers inside the attenuators indicate the attenuation in dB. The room-temperature attenuators before the feedline input optimize the operating range of the generated signals.

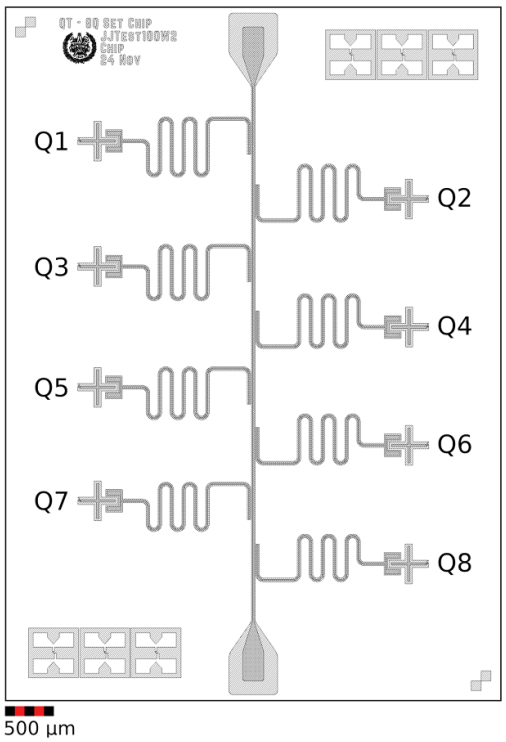

Figure A2. Quantum device chip layout. Qubits $Q_1 - Q_4$ correspond to the *high-dose 1* junction variant in table 1, while $Q_5 - Q_8$ correspond to *high-dose 2* junctions. The two samples S_1 and S_2 were fabricated adjacent to one another on the same wafer.

Appendix B. Device parameters

Table B1 lists the measured and extracted parameters for samples S_1 and S_2 in the two cooldowns *C1* and *C2*. Table B2 lists the acquired decoherence factors.

Table B1. Characteristic parameters of samples S_1 and S_2, which underwent one and two cycles of resistance manipulations, respectively. *C1* and *C2* denote the two cryostat cooldowns. $f_{\mathrm{res},|0\rangle}$ is the resonator frequency when the corresponding qubit is in $|0\rangle$, κ is the energy decay rate of the resonator, η is the transmon anharmonicity, f_{01} is the qubit's $|0\rangle \rightarrow |1\rangle$ transition frequency, and 2χ is the dispersive shift.

	$f_{\mathrm{res},\|0\rangle}$ [GHz]	$\kappa/2\pi$ [kHz]	$\eta/2\pi$ [MHz]		f_{01} [GHz]		2χ [kHz]		Q [-]	
S_1			C1	C2	C1	C2	C1	C2	C2	C2
Q_1	5.9532	818		−214.4	4.8514	4.5518	−3108	−1030	1 676 534	1 302 120
Q_2	6.0659	707	−210.0		4.9853		−1764		1 190 290	
Q_3	6.1935	730		−222.2	4.1680	4.0851	−1024	−411	2 487 886	1 375 136
Q_4	6.3155	692	−210.3		4.9750		−1435		1 500 422	
Q_5	6.4513	767	−202.3		5.5673		−2887		1 014 434	
Q_6	6.5924	812	−204.8	−197.6	5.4177	4.9811	−1671	−899	1 123 330	365 889
Q_7	6.7446	924	−201.7	−207.2	5.3942	5.1232	−1434	−965	1 186 250	1 397 712
Q_8	6.8918	898	−203.2	−205.3	5.5847	5.2863	−1627	−1159	1 122 872	1 116 143
S_2										
Q_1	5.9509	646	−212.7		4.7759		−1495		840 215	
Q_2	6.0668	647								
Q_3	6.1908	754	−216.8	−222.0	4.4353	4.2354	−778	−620	1 337 651	1 341 931
Q_4	6.3127	735								
Q_5	6.4554	777	−207.4		5.1634	4.8590	−1495	−2054	1 297 704	1 860 994
Q_6	6.5811	735								
Q_7	6.7419	815	−208.9		4.9492	4.8039	−857	−574	1 212 784	163 470
Q_8	6.8838	1011								

Table B2. Decoherence times for samples S_1 and S_2 across two cooldowns, *C1* and *C2*. Entries labeled *n/a* indicate data with uncertainties too large to report reliably, while blank entries correspond to qubits that failed. S_2 was resistance-manipulated prior to *C1*, whereas both S_1 and S_2 underwent manipulation prior to *C2*.

		$T_{1,\,C1}$ [μs]	$T_{1,\,C2}$ [μs]	$T^*_{2,\,C1}$ [μs]	$T^*_{2,\,C2}$ [μs]	$T^e_{2,\,C1}$ [μs]	$T^e_{2,\,C2}$ [μs]
S_1	Q_1	55 ± 6	46 ± 7	25 ± 6	23 ± 5	n/a	29 ± 3
	Q_2	38 ± 7		47 ± 3		73 ± 4	
	Q_3	95 ± 17	54 ± 12	34 ± 16	17 ± 4	65 ± 7	62 ± 8
	Q_4	48 ± 10		49 ± 13		72 ± 5	
	Q_5	29 ± 4		38 ± 5		57 ± 4	
	Q_6	33 ± 2	12 ± 1	19 ± 7	4 ± 1	56 ± 5	21 ± 1
	Q_7	35 ± 5	43 ± 8	9 ± 1	40 ± 6	57 ± 7	52 ± 6
	Q_8	32 ± 3	34 ± 7	37 ± 4	37 ± 7	53 ± 6	44 ± 6
S_2	Q_1	28 ± 3		21 ± 4		37 ± 3	
	Q_2						
	Q_3	48 ± 7	50 ± 9	36 ± 16	21 ± 2	66 ± 7	57 ± 7
	Q_4						
	Q_5	40 ± 3	61 ± 11	33 ± 5	14 ± 10	61 ± 4	n/a
	Q_6						
	Q_7	39 ± 5	5 ± 0.1	39 ± 8	1 ± 0.1	67 ± 9	n/a
	Q_8						

Appendix C. Heat exposure post-deposition

Table C1 summarizes the post-deposition thermal processing applied to the fabricated samples. The *low-dose* junctions were fabricated using the PICT process [26], in which the patch-related processing steps were omitted. The *medium-dose* wafer additionally included airbridge fabrication, introducing heating in the additional fabrication steps.

Table C1. Summary of post-deposition heat exposure during fabrication.

Heating step	Temperature [°C]	Duration [min]	Applicable samples
Lift-off after junction deposition.	85	150	All
Resist baking for patch lithography.	160	15	*Medium-dose*, *High-dose*
Patch lift-off.	85	180	*Medium-dose*, *High-dose*
Dicing-protective resist baking.	100	1	All
Final resist removal.	85	15	All
Resist baking for airbridge lithography.	115	1.5	*Medium-dose*
Resist reflow for airbridges.	160	4	*Medium-dose*
Additional resist baking for lithography and dicing.	100	1.7	*Medium-dose*
Additional resist removal.	90	20	*Medium-dose*

Appendix D. Relating resistance to qubit frequency

The normal state resistance of a Josephson junction relates to the energy gap between the transmon qubit's $|0\rangle$ and $|1\rangle$ states through the Josephson energy [25], and ultimately through the Ambegaokar–Baratoff relation [37, 38]. For a transmon qubit with charging energy $E_C = e^2/(2 \cdot C)$ where $4E_C = \frac{(2e)^2}{2C}$ corresponds to the energy of a single Cooper pair stored in the transmon's capacitor [25, 39], and Josephson energy E_J, the transition frequency f_{01} can be approximated [40] to

$$h\,f_{01} = \sqrt{8\,E_\mathrm{J}\,E_\mathrm{C}} - E_\mathrm{C}\,\left(1 + \xi\;1/4 + \xi^2\;21/128\right), \tag{D.1}$$

where $\xi = \sqrt{2\,E_\mathrm{C}/E_\mathrm{J}}$, and h is the Planck constant. The Josephson energy E_J is related to the critical current I_C via

$$E_\mathrm{J} = \frac{\Phi_0}{2\pi}\,I_\mathrm{C} = \frac{\hbar}{2e}\,I_\mathrm{C}, \tag{D.2}$$

where Φ_0 is the magnetic flux quantum and e the electron charge. The critical current I_C relates to the normal state resistance R_N of the junction through the Ambegaokar–Baratoff relation

$$I_\mathrm{C} = \frac{\pi\,\Delta_\mathrm{g}(T)}{2e\,R_\mathrm{N}}\tanh\left(\frac{\Delta_\mathrm{g}(T)}{2k_\mathrm{B}T}\right), \tag{D.3}$$

where $\Delta_\mathrm{g}(T)$ is the superconducting energy gap, k_B is the Boltzmann constant, and T is the superconductor temperature. For a non-manipulated *medium-dose* junction, we measured $\Delta_\mathrm{g}(T \approx 10\ \mathrm{mK}) = 174.3\ \mu\mathrm{eV}$, yielding $\tanh\left(\frac{\Delta_\mathrm{g}(T)}{2k_\mathrm{B}T}\right) \approx 1$ in equation (D.3). We note that our measured superconducting energy gap is close to the textbook number for bulk aluminum $\Delta_\mathrm{g}(T) \approx 178.2\ \mu\mathrm{eV}$ [41], resulting in $\frac{2\Delta_\mathrm{g}(0.01)}{\alpha_\mathrm{BCS}\cdot k_\mathrm{B}} = T_c \approx 1.16$ K, where $\alpha_\mathrm{BCS} = 3.5$ is the ideal gap ratio [42]. For reference, the nominal film thicknesses of this junction are 39 nm for the bottom electrode, and 78 nm for the top electrode.

Substituting equation (D.3) into equation (D.2), and subsequently into equation (D.1), completes a relation between the normal state resistance R_N and the qubit frequency f_{01},

$$hf_{01} = \sqrt{8E_\mathrm{C}\frac{\hbar\pi\,\Delta_\mathrm{g}(T)}{4e^2R_\mathrm{N}}} - E_\mathrm{C}\left(1 + \frac{1}{4}\sqrt{\frac{2E_\mathrm{C}}{\frac{\hbar\pi\,\Delta_\mathrm{g}(T)}{4e^2R_\mathrm{N}}}} + \frac{21}{128}\sqrt{\frac{2E_\mathrm{C}}{\frac{\hbar\pi\,\Delta_\mathrm{g}(T)}{4e^2R_\mathrm{N}}}}\right). \tag{D.4}$$

R_N relates to the room temperature Josephson junction's resistance R. We use a fixed conversion rate $R_N = R\cdot 1.1385$ based on previous measurements taken on a *low-dose* sample [9]. Hence, we can use equation (D.4) to estimate the change in qubit frequency given an induced change in R. We measure the junction's resistance from its I–V characteristics using a voltage sweep from -13 mV to $+13$ mV, a region where the junction is resistor-like [43], fitting the data to a purely linear model $V = R\cdot I$ giving us a high coefficient of determination $r^2 \geq 0.999$.

D.1. Tuning frequency precision from the relaxation offset error

In figure 6(b), the uncertainty in the relaxation fit offset relating ρ_Total to ρ_Active, is approximately $\pm 0.19\%$. This uncertainty directly translates into an imprecision in the qubit frequency, which we estimate here.

We conservatively assume that the relaxation-offset uncertainty extracted from the *low-dose 1* junctions represents an equal or worse case for both *high-dose* variants used as qubit devices, for which we have experimental data. We further assume an energy gap $\Delta_\mathrm{g}(T \approx 10\,\mathrm{mK}) = 174.3\ \mu\mathrm{eV}$, measured on a *medium-dose* junction, and use the room-temperature to normal-state resistance conversion $R_\mathrm{N} = R\cdot 1.1385$, as described in the previous section. We base our estimate for frequency precision on the unmanipulated reference device's *high-dose 2* junctions, using qubits $Q_5 - Q_8$ in table B1, which have a mean transition frequency $f_{01} = 5.4910$ GHz and a mean anharmonicity $\eta/2\pi = -203.0$ MHz. Using [40] with the same ξ from equation (D.1), E_C is given by

$$\frac{\eta}{2\pi} = -E_\mathrm{C} - \frac{9}{16}\left(E_\mathrm{C}\;\xi\right) - \frac{81}{128}\left(E_\mathrm{C}\;\xi^2\right) - \frac{3645}{4096}\left(E_\mathrm{C}\;\xi^3\right) - \frac{46899}{32768}\left(E_\mathrm{C}\;\xi^4\right). \tag{D.5}$$

Enforcing $\eta/2\pi = -203.0$ MHz in equation (D.5) while simultaneously solving (D.4) to $f_{01} = 5.4910$ GHz, creates a bound solution for R. Numerically, we find R to be 5521.4 Ω, resulting in $E_\mathrm{J} = 21.63$ GHz from equations (D.2) and (D.3), and $E_\mathrm{C} = 186.7$ MHz from equation (D.5).

We repeat this procedure for $R \pm 0.19\%$ which yields a frequency error of $5496.6 - 5485.3 = 11.3$ MHz. We therefore assume that the uncertainty associated with the relaxation offset alone imposes a best-case bound of approximately 11.3 MHz on the attainable frequency precision of electrical tuning, under the assumption considered here.

Appendix E. Additional manipulation analysis with secondary trends

This section details additional analysis and observations used to refine the interpretation of resistance changes in our devices. We first address the removal of the initial resistance drop observed in figure 3, which is necessary for fitting the time-dependent resistance using equation (2). We then justify the use of a second order polynomial in equation (2) to model active resistance manipulation. Finally, we supplement figure 4 and table 2 with equivalent results in units of Ωs^{-1} and Ωs^{-2}.

E.1. Resistance drop

The resistance drop is removed from the dataset prior to fitting equation (2). For completeness, the removed resistance drop for each fit is shown as a function of manipulation voltage in figure 3(f), and as a function of the maximum reported resistance change in figure 3(g). We observe no clear dependence of the initial resistance drop on either resistance change or voltage range. The only systematic trend is that *high-dose* devices consistently exhibit a significantly larger drop than the *low-dose* and *medium-dose* devices.

Furthermore, we note that the resistance drop increases with each successive step in the stepped active manipulation experiments. Figure E1 shows ρ_{Drop} as a function of $\rho(t)$ at the start of each manipulation step in figure 7. The initial drop deepens progressively with each step, before the behavior becomes chaotic. At present, we do not have a definitive explanation for this trend.

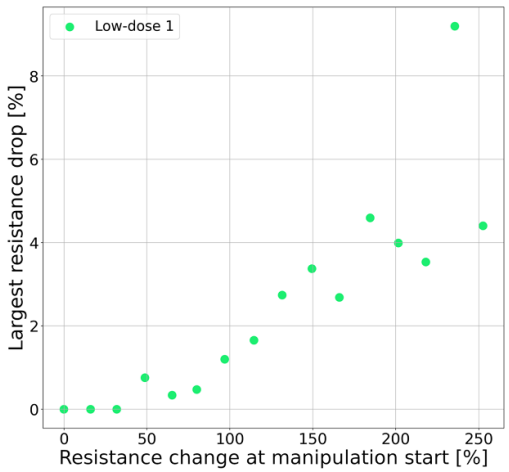

Figure E1. Initial resistance drop at each step during the stepped active manipulation in figure 7, as a function of ρ_{Total} obtained at the previous step. The drop magnitude increases with successive steps, after which the trend becomes irregular.

E.2. Selecting a model for active resistance manipulation

We selected the polynomial model empirically by systematically comparing several candidate models for the resistance change $\rho(t) = R(t)/R(0) - 1$: a second-order polynomial, a third-order polynomial, an exponential, and a power law. Only the second- and third-order polynomials adequately captured the experimentally observed resistance evolution; their RMS errors are summarized in table E1. The mean difference shows that the performance of the third-order polynomial over the second-order polynomial is a few hundredths of percent better, at the cost of adding an additional degree of freedom into the model. We thus adopt the second-order polynomial as the simplest phenomenological model that represents the experimentally observed resistance increase over time, motivated by the fact that the model has fewer free variables at near-equal error.

E.3. Ohmic comparison of resistance change parameters

Tables E2 and E3 present the fit results for $\alpha(V)$ and $\beta(V)$, multiplied by the respective $R(0)$ of each fitted trace, to convert the fractional units into Ωs^{-1} and Ωs^{-2}, respectively. We denote these rescaled parameters as α' and β'. Similarly, table E4 reports the resulting α_0' in units of Ωs^{-1}. For comparison, the characteristic voltage V_0 reported in table 2 is also included.

Table E1. RMS error comparison between the second-order polynomial fit and a third-order polynomial fit for each resistance manipulation fit in figure 3 in the same units as the figure, that is, % resistance change. V_a denotes the manipulation voltage.

V_a [mV]	750	800	850	900	925	950	1000	1050	
				Difference					Mean
Low-dose 1	0.024	0.018	0.004	0.004		0.089			0.028
Low-dose 2	0.006	0.037	0.020	0.051		0.141			0.051
Medium-dose 1				0.0002		0.004	0.044	0.008	0.014
High-dose 1		0.003	0.006	0.003	0.004	0.005	0.00 001		0.004
High-dose 2		0.003	0.003	0.0006	0.0003	0.004	0.0001		0.002
				2nd-order					Mean
Low-dose 1	0.121	0.180	0.219	0.691		0.544			0.351
Low-dose 2	0.079	0.149	0.139	0.307		0.422			0.219
Medium-dose 1				0.078		0.092	0.123	0.129	0.105
High-dose 1		0.072	0.070	0.078	0.084	0.101	0.128		0.088
High-dose 2		0.066	0.067	0.088	0.083	0.086	0.095		0.081
				3rd-order					Mean
Low-dose 1	0.097	0.162	0.214	0.686		0.455			0.323
Low-dose 2	0.072	0.112	0.119	0.256		0.281			0.170
Medium-dose 1				0.078		0.088	0.078	0.121	0.092
High-dose 1		0.069	0.064	0.075	0.080	0.097	0.128		0.085
High-dose 2		0.063	0.063	0.088	0.083	0.082	0.095		0.079

Table E2. Extracted α' and β' parameters for the *low-dose* devices.

Voltage	Low-dose 1 α' [mΩs^{-1}]	Low-dose 1 β' [$\mu\Omega$s^{-2}]	Low-dose 2 α' [mΩs^{-1}]	Low-dose 2 β' [$\mu\Omega$s^{-2}]
750 mV	2930 ± 150	-2600 ± 500	800 ± 50	-328 ± 23
800 mV	6420 ± 180	-5700 ± 800	1560 ± 40	-1000 ± 170
850 mV	12100 ± 600	-8230 ± 250	3920 ± 17	-2460 ± 80
900 mV	22600 ± 500	-16500 ± 2100	8480 ± 210	-4660 ± 80
950 mV	50300 ± 400	-33000 ± 1500	17960 ± 120	-7900 ± 500

Table E3. Extracted α' and β' parameters for the *medium-dose* and *high-dose* devices.

Voltage	Medium-dose 1 α' [mΩs^{-1}]	Medium-dose 1 β' [$\mu\Omega$s^{-2}]	High-dose 1 α' [mΩs^{-1}]	High-dose 1 β' [$\mu\Omega$s^{-2}]	High-dose 2 α' [mΩs^{-1}]	High-dose 2 β' [$\mu\Omega$s^{-2}]
800 mV			80.9 ± 2.6	238 ± 11	130 ± 15	-174 ± 7
850 mV			159 ± 19	259 ± 8	073 ± 13	185 ± 6
900 mV	1990 ± 50	-2000 ± 270	543 ± 17	-76 ± 8	255 ± 11	-35 ± 4
925 mV			602 ± 15	153 ± 6	446 ± 5	26.6 ± 1.3
950 mV	3460 ± 30	-3090 ± 120	780 ± 230	-162 ± 14	632 ± 10	-173 ± 5
1000 mV	6762 ± 23	-4710 ± 100	2280 ± 160	-950 ± 60	1700 ± 100	-217 ± 5
1050 mV	10449 ± 21	-4870 ± 90				

Table E4. Fit parameter α_0' and the corresponding characteristic voltage V_0. This voltage represents the additional voltage required for the linear rate of resistance change, to increase by a factor e.

	Low-dose 1	Low-dose 2	Medium-dose 1	High-dose 1	High-dose 2
α_0' [$\mu\Omega$s^{-1}]	98.2 ± 2.3	21.5 ± 1.3	108.4 ± 3.3	0.0650 ± 0.0005	0.0253 ± 0.0005
V_0 [mV]	72.5 ± 2.4	70.4 ± 3.4	91.4 ± 4.3	57.5 ± 5.0	55.3 ± 3.1

Appendix F. Residual analysis between relaxation models

To characterize the relaxation growth, we compare the logarithmic model in equation (4) with a power-law description,

$$y(t) = a + c \cdot t^{d}. \tag{F.1}$$

We evaluate the mean and variance of the residuals Δk, Δm between the fitted curves and the measured data. For the logarithmic model, the mean residuals are $\langle \Delta k \rangle = -1.42 \cdot 10^{-5}$ and $\langle \Delta_m \rangle = -8.59 \cdot 10^{-6}$, with variances $2.04 \cdot 10^{-5}$ and $1.63 \cdot 10^{-3}$, respectively. In contrast, the power-law model yields larger residuals, with mean values $\langle \Delta k \rangle = -9.16 \cdot 10^{-5}$ and $\langle \Delta m \rangle = -1.06 \cdot 10^{-4}$ and variances $5.16 \cdot 10^{-5}$ and $2.18 \cdot 10^{-3}$. The consistently smaller residuals and variances indicate that the relaxation growth is better described by a logarithmic dependence than by a power law. In all fits, we enforced a minimum bound for a being 1 corresponding to $\rho_{\mathrm{Total}}(t_{\mathrm{Stop}})/\rho_{\mathrm{Active}}(t_{\mathrm{Stop}}) = 1$, as no relaxation has yet occurred at the stopping time.

Appendix G. A thermally activated process

The term *electrical annealing* is commonly used to describe the resistance manipulation process studied in this work. However, the terminology *annealing* can be misleading, as there is strong evidence that the underlying physical process does not primarily rely on heating the junction to conventional annealing temperatures. Instead, the experimental picture that emerges is that electrical tuning is fundamentally a thermally activated process, in which the electric field plays an essential role.

To demonstrate how the manipulation process is influenced by temperature, we performed an ad-hoc experiment. We performed resistance manipulation at room temperature, after which the junction was allowed to relax while submerged in liquid nitrogen. The experiments were carried out in an aluminum enclosure, surrounded by a styrofoam insulating layer, mounted onto the manual probe station. The enclosure was designed to be filled with liquid nitrogen through a dedicated inlet. A test chip containing *low-dose* Josephson junctions was glued to the bottom of the box using BF-6 Bakelite phenol-formaldehyde adhesive, and a Si-540 silicon diode thermometer was mounted nearby for temperature monitoring via a spare channel of the source-measurement unit. Electrical connections to the sample were made by inserting the manual station's probe needles through a large opening in the box lid, which also allowed nitrogen boil-off to escape and thereby suppressed condensation on the sample. A secondary gas inlet enabled controlled warmup using room-temperature nitrogen gas and provided a slight overpressure to mitigate moisture accumulation. Significant thermal contraction and expansion of the probe needles during cooldown and warmup required repeated manual realignment to maintain electrical contact with the sample.

Figure G1(a) shows an electrical tuning experiment of a 183-day-old *low-dose* junction, where the device is submerged in liquid nitrogen immediately after resistance manipulation, so that relaxation occurs at lower temperatures. Remarkably, no resistance change is observed while the junction remains cold.

To further emphasize that the relaxation-induced resistance change halts at low temperature, we normalize the measured resistance to its room-temperature equivalent using an approximation to Simmon's model for tunneling through a thin insulator barrier,

$$G(T) = G_0 \cdot \left(1 + \left(\frac{T}{T_0}\right)^2\right), \tag{G.1}$$

where G_0 and T_0 are the characteristic conductance and characteristic temperature, respectively. This model is expected to be applicable since the junction never becomes superconducting during the experiment, and behaves as a metal–insulator-metal junction with a negative temperature coefficient. We find a conversion between the room-temperature conductance and the cryogenic conductance,

$$G_{\mathrm{RT}}(T) = G_{\mathrm{Cryo}}(T) \cdot \left(\frac{G_0 \cdot \left(1 + \left(\frac{297[\mathrm{K}]}{T_0}\right)^2\right)}{G_0 \cdot \left(1 + \left(\frac{T}{T_0}\right)^2\right)}\right), \tag{G.2}$$

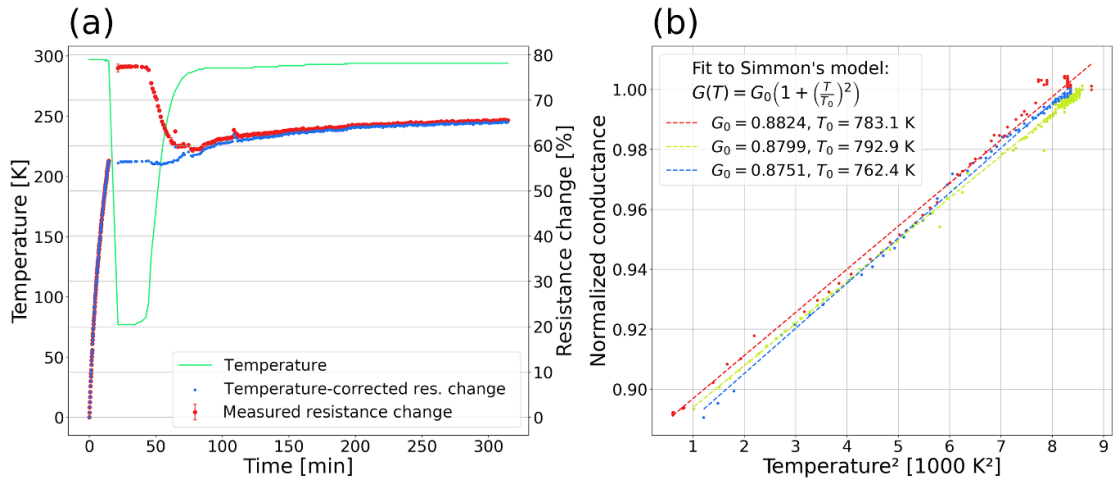

Figure G1. (a) Electrical tuning of a Josephson junction with the relaxation performed in liquid nitrogen. No resistance change is observed while the junction remains cold, a result further emphasized by comparison with the temperature-corrected resistance trace shown as blue points. (b) Determination of the average characteristic temperature $\langle T_0 \rangle$ and normalized conductance $\langle G_0 \rangle$ used for the Simmons-model correction in equation (G.2), extracted from three liquid-nitrogen cooldowns in which temperature and conductance were monitored for three *low-dose* junctions.

where $1/G_{\mathrm{Cryo}} = R$ is the resistance of the junction as we measure it in-situ. Both G_0 and T_0 are determined experimentally in figure G1(b), where three *low-dose* junctions are cooled down, while their resistance and temperature are continuously monitored without performing any electrical tuning. Fitting these three datasets to equation (G.1) yields an averaged normalized conductance $\langle G_0 \rangle = 0.8791$, and an averaged $\langle T_0 \rangle = 779.5$ K. G_0 would, in principle, correspond to the zero-temperature conductance of the junction; its inverse gives

$$1/\langle G_0 \rangle = R/R_{\mathrm{N}} = 1.1375, \tag{G.3}$$

in close agreement with the R/R_{N} factor 1.1385 used throughout this work. Using $\langle T_0 \rangle$ in equation (G.2), figure G1(a) shows the resulting temperature-corrected resistance, confirming that resistance relaxation is effectively frozen out at cryogenic temperature. Moreover, resistance relaxation resumes as the device thaws. It should also be mentioned that electrical tuning itself is known to speed up at elevated temperatures [23].

We initially suspected that the resistance change observed during active manipulation arises from localized Joule heating at the junction's metal–insulator interface, caused by power dissipation $P = V_{\mathrm{drop}} \cdot I$. In [43, figure 4.9], this hypothesis was tested by simulating the localized heating in a cross-style Josephson junction [44] under DC manipulation. For a representative case of $V_{\mathrm{a}} = 0.9$ V applied for 10 min, the junction dissipates approximately 110 μW at the Al-AlO_x interface. Assuming that 10% of the junction area participates in tunneling [28], the resulting tunnel current is 120 μA, corresponding to a simulated local temperature rise of ∼4 K. This result is an order of magnitude below the levels required for conventional thermal annealing, and is also consistent with a recent study reporting ∼8 K local heating in comparable junctions [45].

These results raise the question of whether the relaxation process is fundamentally distinct from, or closely related to, natural aging. Aging studies of Josephson junctions [15, 29] show that aging slows at lower temperatures, with their glassy relaxations showing the same trend [27]. Both aging and relaxation also share in common that subjecting the sample to sufficient heat halts further aging [15], as well as the ability to change resistance from electrical tuning [24]. While there may be other interpretations that we cannot rule out, our measurements in this work are consistent with the following model. The tunnel barrier can be described by an energy landscape containing many metastable local minima. During natural aging, thermal fluctuations at room temperature provide a finite probability for atoms, defects etc to overcome local activation barriers and relax toward lower-energy configurations, thereby increasing the junction resistance. Electrical manipulation could then temporarily modify the energy landscape, the electric field then lowers certain activation barriers sufficiently for room-temperature thermal energy to drive transitions that would otherwise occur only on very long timescales through natural aging. This model is also consistent with the observations reported in [24] where the claim was that subjecting the junctions to thermal treatment, lowers the ability to perform ABAA, and even removing

any ability to perform ABAA if heating junctions to sufficiently high temperature. Such behavior would be expected if the system approaches a global energy minimum by thermal fluctuations, leaving fewer accessible metastable states available for electrically induced rearrangement. We perform electrical tuning on samples that have aged for multiple months, further suggesting that the active manipulation accesses configurations that are not reached through natural aging alone. In active manipulation, the extracted characteristic voltages V_0, in equation (3), have values in the range 55–91 mV; these values are notably comparable to, but larger than, the thermal voltage at room temperature $V_T \approx 25$ mV. This observation is consistent with the interpretation outlined above. The observation reported in [23] that alternating the pulse polarity enhances the range and rate of resistance change could be explained due to enabling transitions out of metastable configurations that become energetically unfavorable under the reversed field direction.

Recent hypotheses [23, 33] speculate that electrical tuning is related to field-assisted oxidation through the Cabrera–Mott mechanism [34]. Within this frame, electrical tuning accelerates the intrinsic relaxation dynamics of the junction not through heating, but by providing an electric-field-driven impulse that promotes ionic rearrangement toward a more stable configuration. However, this interpretation must be reconciled with experimental results showing that Cabrera–Mott oxidation increases as the temperature is lowered [46], in contrast to observations that electrical tuning speeds up with increased temperature.

Appendix H. Dielectric breakdown

Figure H1 shows dielectric breakdown characteristics of *high-dose* junctions. In figure H1(a) the automated probe station was used to apply a current ramp to 119 junctions with areas ranging from 150 nm × 150 nm to 600 nm × 600 nm, while monitoring the voltage across them. The breakdown voltage V_{break} is defined as the highest voltage measured before the resistance dropped below 260 Ω, a threshold determined empirically as the upper bound for the short-circuit resistance of a failed junction. For junctions with electrode widths between 400 nm and 600 nm, we consistently observed $V_{\text{break}} \approx 1.1$ V. As shown in figure H1(b), smaller junctions exhibit increased scatter in both breakdown voltage and resistance-area product, reflecting increased measurement uncertainty and device-to-device variability at reduced dimensions. These results indicate that, for each wafer, dielectric breakdown measurements on sacrificial junctions are essential for establishing safe upper bounds on the voltage amplitude used during electrical tuning.

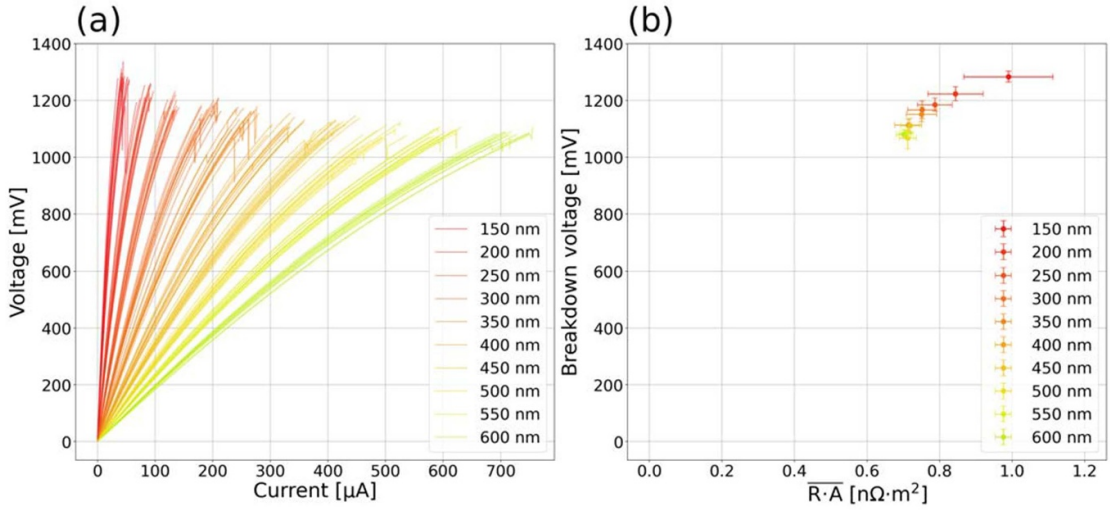

Figure H1. Current-ramped dielectric breakdown measurements performed on sacrificial Josephson junctions from the *high-dose* wafer. (a) Individual *I*–*V* curves for 119 junctions of different sizes. (b) Breakdown voltage as a function of the mean resistance-area product. The legends show the electrode width of the junctions.

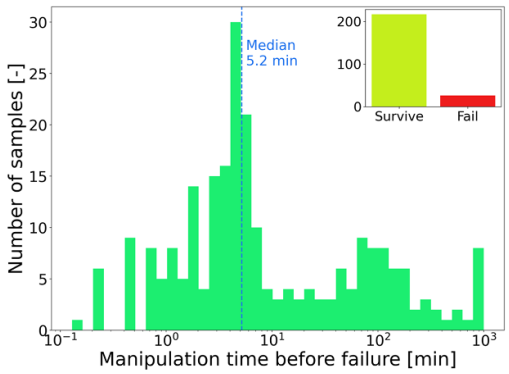

Figure H2. Survival duration analysis of all junction variants that failed at any point during active manipulation with $V_a = 0.85$ V. For a junction failing in this work, the median survival time is 5.2 min. Across all junction variants studied, the overall survival rate is 89.3%, with the 10-percentile being 1.0 min and the 90-percentile being 167.0 min.

H.1. Survival duration during tuning

Figure H2 shows a histogram of the survival duration for $n = 243$ junctions that at any point broke during manipulation, using the regular manipulation procedure outlined in section 2.1. All failures resulted from a short circuit through the junction, defined as measuring a junction resistance of less than 260 Ω. The data includes results from stepped active manipulation experiments, where we counted only the first step of the manipulation since this step is identical to a regular manipulation. We achieve a survival rate of 89.3%. We believe that the electrical tuning protocol requires identifying a safe tuning voltage for junctions of that particular wafer. In our work, selecting $V_a = 0.85$ V for all junction variants, while consistent across all variants studied, is not a one-size-fits-all; as was shown in table 2, the rate of resistance change spans multiple orders of magnitude even for the same manipulation voltage.

ORCID iDs

Christian Križan 0000-0002-5059-7998
Maurizio Toselli 0009-0008-8655-6873
Irshad Ahmad 0000-0003-2607-0093
Hadi Khaksaran 0000-0002-2404-1769
Marcus Rommel 0000-0002-3026-3907
Nermin Trnjanin 0009-0006-6911-5182
Janka Biznárová 0000-0002-8887-8816
Mamta Dahiya 0000-0001-6824-769X
Emil Hogedal 0009-0008-1447-5484
Halldór Jakobsson 0009-0007-6824-3251
Andreas Nylander 0000-0002-9724-1892
Jonas Bylander 0000-0003-4521-710X
Per Delsing 0000-0002-1222-3506
Giovanna Tancredi 0000-0002-3628-8398

References

[1] Blais A, Grimsmo A L, Girvin S M and Wallraff A 2021 *Rev. Mod. Phys.* **93** 025005
[2] Josephson B D 1962 *Phys. Lett.* **1** 251–3
[3] Anderson P W and Rowell J M 1963 *Phys. Rev. Lett.* **10** 230–2
[4] Muthusubramanian N, Finkel M, Duivestein P, Zachariadis C, van der Meer S L M, Veen H M, Beekman M W, Stavenga T, Bruno A and DiCarlo L 2024 *Quantum Sci. Technol.* **9** 025006
[5] Moskalev D O, Zikiy E V, Pishchimova A A, Ezenkova D A, Smirnov N S, Ivanov A I, Korshakov N D and Rodionov I A 2023 *Sci. Rep.* **13** 4174
[6] Osman A, Fernández-Pendás J, Warren C, Kosen S, Scigliuzzo M, Frisk Kockum A, Tancredi G, Fadavi R A and Bylander J 2023 *Phys. Rev. Res.* **5** 043001
[7] Kreikebaum J M, O'Brien K P, Morvan A and Siddiqi I 2020 *Supercond. Sci. Technol.* **33** 06LT02
[8] Pishchimova A A, Smirnov N S, Ezenkova D A, Krivko E A, Zikiy E V, Moskalev D O, Ivanov A I, Korshakov N D and Rodionov I A 2023 *Sci. Rep.* **13** 6772

[9] Osman A 2024 Scaling superconducting quantum processors: coherence, frequency targeting and crosstalk *PhD Dissertation* Chalmers University of Technology (available at: https://research.chalmers.se/en/publication/543784)
[10] Hertzberg J B, Orcutt J S, Paik H, Rosenblatt S and Sandberg M O 2025 Frequency tuning of multi-qubit systems *US Patent* US12414482B2 (available at: https://patents.google.com/patent/US12414482B2/en)
[11] Hertzberg J B *et al* 2021 *npj Quantum Inf.* **7** 129
[12] Shao D, Brink M, Solgun F and Hertzberg J B 2021 Qubit frequency tuning structures and fabrication methods for flip chip quantum computing devices *US Patent* US10903412B2 (available at: https://patents.google.com/patent/US10903412)
[13] Pavolotsky A B, Dochev D and Belitsky V 2011 *J. Appl. Phys.* **109** 024502
[14] Lehnert T, Billon D, Grassl C and Gundlach K H 1992 *J. Appl. Phys.* **72** 3165–8
[15] Koppinen P J, Väistö L M and Maasilta I J 2007 *Appl. Phys. Lett.* **90** 053503
[16] Granata C, Vettoliere A, Petti L, Rippa M, Ruggiero B, Mormile P and Russo M 2007 *Appl. Phys. Lett.* **90** 232503
[17] van der Meer S 2021 Improving frequency targeting of transmon qubits through automated laser annealing *Master's Thesis* Delft University of Technology (available at: https://resolver.tudelft.nl/uuid:a1c52f6b-4882-4d4b-8423-4056973efa5e) (Accessed 11 July 2025)
[18] Zhang E J *et al* 2022 *Sci. Adv.* **8** eabi6690
[19] Groves T R 1996 *J. Vac. Sci. Technol. B* **14** 3839–44
[20] Balaji Y, Acharya N, Armstrong R, Crawford K G, Danilin S, Dixon T, Kennedy O W, Pothuraju R D, Shahbazi K and Shelly C D 2024 Electron-beam annealing of Josephson junctions for frequency tuning of quantum processors (arXiv:2402.17395)
[21] University of Chicago 2022 Technologies for tuning superconducting Josephson junctions *US Patent* US20220140221A1 (available at: https://patents.google.com/patent/US20220140221A1)
[22] Nylander A and Rommel M 2024 System and method for trimming metal-insulator-metal junctions *International Patent Application WO2024225965A1* (World Intellectual Property Organization) (available at: https://patents.google.com/patent/WO2024225965A1/en)
[23] Pappas D P *et al* 2024 *Commun. Mater.* **5** 150
[24] Chaves K, Iaia V, Rash D, Rosen Y, Alegria L and Abelson A 2025 Oral: expanded parameter search of alternating-bias assisted annealing (ABAA) *Presented by Loren Alegria at the APS Global Physics Summit* (Session MAR-C18: Advanced Fabrication for Superconducting Qubits), (Anaheim Convention Center), Room 162 (Level 1) (17 March 2025)
[25] Koch J, Yu T M, Gambetta J, Houck A A, Schuster D I, Majer J, Blais A, Devoret M H, Girvin S M and Schoelkopf R J 2007 *Phys. Rev. A* **76** 042319
[26] Osman A, Simon J, Bengtsson A, Kosen S, Krantz P, Lozano D P, Scigliuzzo M, Delsing P, Bylander J and Fadavi R A 2021 *Appl. Phys. Lett.* **118** 064002
[27] Nesbitt J R and Hebard A F 2007 *Phys. Rev. B* **75** 195441
[28] Zeng L J, Nik S, Greibe T, Krantz P, Wilson C M, Delsing P and Olsson E 2015 *J. Phys. D: Appl. Phys.* **48** 395308
[29] Bladh K 2005 Quantum coherence in the single Cooper pair box *PhD Dissertation* Chalmers University of Technology
[30] Pappas D, Field M, Sete E A, Mutus J Y and Wang X 2025 Voltage-assisted annealing to alter tunnel junction properties *US Patent* US20250204275A1 figures 5b, 8 and 9 (available at: https://patents.google.com/patent/US20250204275A1)
[31] Herrmann L B 2024 Simulations and measurements of high-frequency transmons for a quantum transduction experiment *Master's Thesis ETH Zürich* (available at: https://hyqu.ethz.ch/publications/master-theses.html) (Accessed 22 April 2026)
[32] Križan C *et al* 2025 *New J. Phys.* **27** 074507
[33] Wang X *et al* 2024 Precision frequency tuning of tunable transmon qubits using alternating-bias assisted annealing *2024 IEEE Int. Conf. on Quantum Computing and Engineering (QCE)* vol 01 (IEEE) pp 1315–23
[34] Cabrera N and Mott N F 1949 *Rep. Prog. Phys.* **12** 163–84
[35] Tholén M O *et al* 2022 *Rev. Sci. Instrum.* **93** 104711
[36] Tholén M O, Borgani R, Križan C, Bylander J and Haviland D B 2023 Characterization and benchmarking of a phase-sensitive two-qubit gate using direct digital synthesis (arXiv:2308.08893)
[37] Ambegaokar V and Baratoff A 1963 *Phys. Rev. Lett.* **10** 486–9
[38] Ambegaokar V and Baratoff A 1963 *Phys. Rev. Lett.* **11** 104–104
[39] Rahamim J 2019 Development of a coaxial circuit QED architecture for quantum computing *PhD Dissertation* University of Oxford (available at: https://ora.ox.ac.uk/objects/uuid:c3311eef-7f31-4cfe-afd7-f3605b73ab36)
[40] Didier N, Sete E A, da Silva M P and Rigetti C 2018 *Phys. Rev. A* **97** 022330
[41] Mangin P and Kahn R 2017 *Cooper Pairs—Principal Results of BCS Theory* (Springer) p 214
[42] Bardeen J, Cooper L N and Schrieffer J R 1957 *Phys. Rev.* **108** 1175–204
[43] Toselli M 2024 Post-fabrication frequency tuning in superconducting transmon qubits *Master's Thesis* Chalmers University of Technology (available at: http://hdl.handle.net/20.500.12380/308503)
[44] Potts A, Parker G, Baumberg J and de Groot P 2001 *IEE Proc. Sci. Meas. Technol.* **148** 225–8
[45] Kennedy O W, Cole J H and Shelly C D 2025 *Phys. Rev. Lett.* **135** 196202
[46] Cai N, Zhou G, Müller K and Starr D E 2012 *Appl. Phys. Lett.* **101** 171605
[47] Križan C and Toselli M 2025 Dataset and code used for Electrical post-fabrication tuning of aluminum Josephson junctions at room-temperature *Zenodo* https://doi.org/10.5281/zenodo.17817323